

EVOLUTION OF THE RADIUS VALLEY AROUND LOW MASS STARS FROM *KEPLER* AND *K2*

RYAN CLOUTIER^{1,2} AND KRISTEN MENOU^{3,2,4}

Draft version February 24, 2020

ABSTRACT

We present calculations of the occurrence rate of small close-in planets around low mass dwarf stars using the known planet populations from the *Kepler* and *K2* missions. Applying completeness corrections clearly reveals the radius valley in the maximum a-posteriori occurrence rates as a function of orbital separation and planet radius. We measure the slope of the valley to be $r_{p,\text{valley}} \propto F^{-0.060 \pm 0.025}$ which bears the opposite sign from that measured around Sun-like stars thus suggesting that thermally driven atmospheric mass loss may not dominate the evolution of planets in the low stellar mass regime or that we are witnessing the emergence of a separate channel of planet formation. The latter notion is supported by the relative occurrence of rocky to non-rocky planets increasing from 0.5 ± 0.1 around mid-K dwarfs to 8.5 ± 4.6 around mid-M dwarfs. Furthermore, the center of the radius valley at $1.54 \pm 0.16 R_\oplus$ is shown to shift to smaller sizes with decreasing stellar mass in agreement with physical models of photoevaporation, core-powered mass loss, and gas-poor formation. Although current measurements are insufficient to robustly identify the dominant formation pathway of the radius valley, such inferences may be obtained by *TESS* with $\mathcal{O}(85,000)$ mid-to-late M dwarfs observed with 2-minute cadence. The measurements presented herein also precisely designate the subset of planetary orbital periods and radii that should be targeted in radial velocity surveys to resolve the rocky to non-rocky transition around low mass stars.

1. INTRODUCTION

NASA's *Kepler* space telescope has discovered thousands of exoplanets over its lifetime and consequently enabled robust investigations of the occurrence rate of planets within our galaxy. One striking outcome of such studies was that the so-called super-Earths and sub-Neptunes—whose radii span sizes intermediate between those of the Earth and Neptune—represent the most common type of planet around Sun-like stars and M dwarfs alike (e.g. Youdin 2011; Howard et al. 2012; Dressing & Charbonneau 2013; Fressin et al. 2013; Petigura et al. 2013; Morton & Swift 2014; Dressing & Charbonneau 2015; Mulders et al. 2015a; Gaidos et al. 2016; Fulton et al. 2017; Hardegree-Ullman et al. 2019). Furthermore, mass measurements of many of these transiting planets via transit-timing variations or precision radial velocity measurements revealed that the majority of planets smaller than $\sim 1.6 R_\oplus$ are consistent with having bulk rocky compositions (e.g. Weiss & Marcy 2014; Dressing et al. 2015; Rogers 2015).

Early studies of the *Kepler* planet population hinted that planets at small orbital separations exhibited a bimodal radius distribution (e.g. Owen & Wu 2013)—commonly referred to as the radius valley—that is thought to be representative of a population of small, predominantly rocky planets plus a population of inflated non-rocky planets that have retained significant H-

He envelopes. Consequently, numerous studies of planet formation and evolution sought to explain the apparent bimodality. One such proposed mechanism is that of photoevaporation wherein the gaseous envelopes of small close-in planets may be stripped by X-ray and extreme ultraviolet (XUV) radiation from their host stars during the first ~ 100 Myrs of the planet's lifetime (Jackson et al. 2012; Owen & Wu 2013; Jin et al. 2014; Lopez & Fortney 2014; Chen & Rogers 2016; Owen & Wu 2017; Jin & Mordasini 2018; Lopez & Rice 2018). The radius valley may also be explained by core-powered mass loss wherein the luminosity from a planetary core's primordial energy reservoir from formation drives atmospheric escape over Gyr timescales (Ginzburg et al. 2018; Gupta & Schlichting 2019a,b). Impact erosion by planetesimals may also drive the emergence of the radius valley either by atmospheric stripping or by the growth of volatile-rich secondary atmospheres (Shuvalov 2009; Schlichting et al. 2015; Wyatt et al. 2019). An alternative explanation to the processing of primordial atmospheres is the formation of distinct rocky and non-rocky planet populations with the former invoking gas-poor formation wherein gas accretion is delayed by dynamical friction whilst the planetary core is still embedded within the protoplanetary disk until a point at which the gaseous disk has almost completely dissipated after just a few Myrs (Lee et al. 2014; Lee & Chiang 2016; Lopez & Rice 2018).

Observational tests of the aforementioned theoretical frameworks have become feasible in recent years due to the precise refinement of measured planet radii following improved stellar host characterization via spectroscopy, asteroseismology, and *Gaia* parallaxes (e.g. Fulton et al. 2017; Berger et al. 2018; Fulton & Petigura 2018; Van Eylen et al. 2018; Martinez et al. 2019). Each of these independent studies clearly resolved the radius valley among small close-in planets orbiting Sun-like stars. A variety of trends were also observed in either the raw

ryan.cloutier@cfa.harvard.edu

¹ Center for Astrophysics | Harvard & Smithsonian, 60 Garden Street, Cambridge, MA, 02138, USA

² Dept. of Astronomy & Astrophysics, University of Toronto, 50 St. George Street, Toronto, ON, M5S 3H4, Canada

³ Physics & Astrophysics Group, Dept. of Physical & Environmental Sciences, University of Toronto Scarborough, 1265 Military Trail, Toronto, ON, M1C 1A4, Canada

⁴ Dept. of Physics, University of Toronto, 60 St. George Street, Toronto, ON, M5S 1A7, Canada

or in the completeness-corrected (i.e. the occurrence rate) distributions. Firstly, the location of the radius valley around FGK stars is period-dependent with slope $d \log r_p / d \log P \sim -0.1$ (Van Eylen et al. 2018; Martinez et al. 2019). This result is consistent with both photo-evaporation and core-powered mass loss models but is largely inconsistent with the late formation of terrestrial planets in a gas-poor environment. Secondly, the feature locations (i.e. the weighted average radius of the peaks and valley) appear to exist at smaller planet radii with decreasing stellar mass (Fulton & Petigura 2018; Wu 2019).

In this study, we extend the investigation of the occurrence rate of small close-in planets to the low mass stellar regime by considering planetary systems hosted by low mass dwarf stars later than mid-K dwarfs. The empirical population of known planets in this stellar mass regime features nearly an order of magnitude fewer planets than around Sun-like stars thus making the clear detection of the radius valley more difficult and at a lower signal-to-noise. This fact is clearly evidenced in the empirical *Kepler* planet population for which the radius valley around Sun-like stars ($T_{\text{eff}} \in [4700, 6500]$ K) is clearly exhibited whereas a similar feature around low mass stars ($T_{\text{eff}} < 4700$ K) is not easily discernible by eye (Figure 1 based on the data from Berger et al. 2018). Herein we leverage the precise stellar parallaxes from the *Gaia* DR2 for low mass stars observed by *Kepler* and *K2* to refine the stellar parameters and compute precise occurrence rates of close-in planets with the goal of resolving the radius valley and accurately measuring the locations of its features and their uncertainties. Although it is unlikely that a single physical mechanism is solely responsible for sculpting the radius valley, investigating the evolution of the valley features with stellar mass can allude to which process—if any—dominates the evolution of close-in planets.

In Sects. 2 and 3 we define our stellar sample from *Kepler* and *K2* and compile our sample of confirmed planets from each mission. In Sect. 4 we derive the transiting planet detection completeness and use those results to calculate the occurrence rate of small close-in planets in which the structure of the radius valley around low mass stars is resolved (Sect. 5). In Sect. 6 we compare our results to model predictions and to results from planet population studies around Sun-like stars. Sect. 7 presents a discussion of our results and their implications followed by a summary of our main findings in Sect. 8.

2. LOW MASS DWARF STELLAR SAMPLE

The goal of this study is to extend measurements of the occurrence rate of close-in planets to planetary systems around low mass dwarf stars with effective temperatures $T_{\text{eff}} < 4700$ K, where 4700 K was the lower limit on T_{eff} that was considered in the California Kepler Survey (CKS; Fulton et al. 2017). This adopted temperature threshold approximately corresponds to spectral types later than K3.5V (Pecaut & Mamajek 2013). In the following subsections we define our stellar samples from each of *Kepler* or *K2*.

2.1. *Kepler* stellar sample

Following the release of *Gaia* DR2 (Lindegren et al. 2018), Berger et al. (2018) cross-matched *Kepler* target

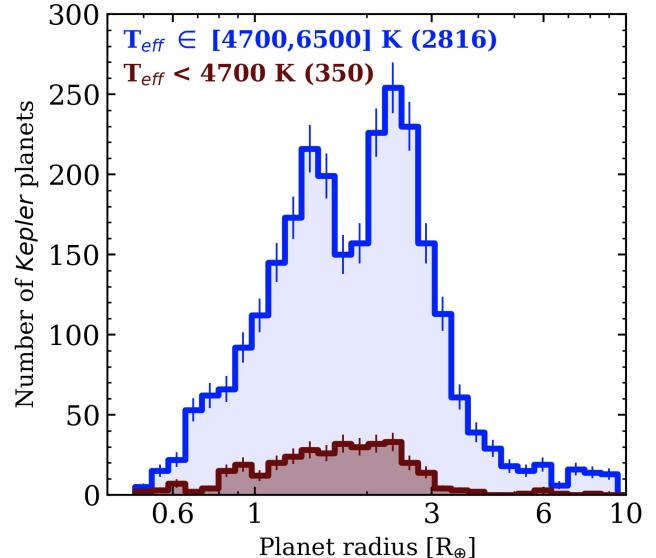


FIG. 1.— Empirical distributions of *Kepler* planet radii. Histograms of *Kepler* planet radii from Berger et al. (2018) for planets with host stellar effective temperatures $T_{\text{eff}} \in [4700, 6500]$ K (blue) and $T_{\text{eff}} < 4700$ K (red). The former subset of 2816 planets corresponds to the effective temperature range considered in the California Kepler Survey (Fulton et al. 2017) wherein the radius valley is clearly resolved in the empirical distribution even without completeness corrections. A similar bimodal structure is not resolved in the empirical distribution of the latter subset around low mass stars due in-part to the relatively poor counting statistics with just 350 planets.

stars with DR2 and compiled a catalog of stellar parallaxes ϖ , 2MASS K_s -band magnitudes, and spectroscopic measurements of T_{eff} , $\log g$, and $[\text{Fe}/\text{H}]$ for $\sim 178,000$ stars observed as part of the primary *Kepler* mission. Spectroscopic measurements were obtained from either the Data Release 25 (DR25) Kepler Stellar Properties Catalog (KSPC; Mathur et al. 2017), the California Kepler Survey (CKS; Petigura et al. 2017) where available, and T_{eff} values for stars with $T_{\text{eff}} < 4000$ K were compiled from Gaidos et al. (2016). The full set of available stellar parameters were used as input within the spectral classification code `isoclassify` (Huber et al. 2017) to calculate stellar luminosities. The resulting luminosity values were consequently combined with T_{eff} measurements to refine the stellar radii using the Stefan-Boltzmann law for the majority of *Kepler* FGK stars. However, bolometric corrections for *Kepler* M dwarfs with $T_{\text{eff}} < 4100$ K and absolute K_s -band magnitudes $M_{K_s} > 3$ are known to suffer significant inaccuracies owing to incomplete molecular line lists (Mann et al. 2015). For these stars, Berger et al. (2018) instead adopted the empirically-derived M dwarf radius-luminosity relation from Mann et al. (2015) to refine the M dwarf stellar radii. Berger et al. (2018) also combined T_{eff} and the luminosity measurements to derive stellar evolutionary flags aimed at classifying stars as either a dwarf, a subgiant, or a red giant.

Stellar masses M_s are not reported by Berger et al. (2018). In order to study the *Kepler* planet population as a function of M_s we derive M_s values given the measured stellar radii R_s and using the mass-radius relation from Boyajian et al. (2012) applicable to both K and M dwarfs. Boyajian et al. (2012) acquired interferometric measurements with the *CHARA* array of 21 nearby K and M dwarfs to measure the angular size of each stellar

disk at the level of $\lesssim 5\%$. Their stellar sample was supplemented by twelve literature measurements of R_s from interferometry. Mass measurements were then derived using the K_s -band mass-luminosity relation from Henry & McCarthy (1993) which was valid for their full stellar sample spanning 0.13–0.90 R_\odot . Boyajian et al. (2012) parameterized the stellar mass-radius relationship as a quadratic in M_s and reported values and uncertainties for each polynomial coefficient. Here, we sample each coefficient its independent Gaussian probability density function (PDF), along with each star’s R_s from its measurement uncertainty, to derive the M_s PDF for all of the low mass dwarfs in our preliminary *Kepler* sample.

We define our final *Kepler* stellar sample by focusing on stars that satisfy the following criteria:

1. *Kepler* magnitude $K_p < 16$,
2. $T_{\text{eff}} - \sigma_{T_{\text{eff}}} \leq 4700$ K,
3. $R_s - \sigma_{R_s} \leq 0.8 R_\odot$,
4. $M_s - \sigma_{M_s} \leq 0.8 M_\odot$, and
5. and an evolutionary flag corresponding to a dwarf star.

We also only consider *Kepler* stars for which reliable completeness products from DR25 are available (see Sect. 4.1). Based on these criteria, we retrieve 3965 low mass *Kepler* stars whose stellar parameters are depicted in Figure 2. In our *Kepler* sample, the *Kepler* magnitudes span $K_p \in [10.35, 16.00]$ with a median value of 15.16, effective temperatures span $T_{\text{eff}} \in [3154, 4870]$ K with a median value of 4394 K, stellar radii span $R_s \in [0.17, 0.87] R_\odot$ with a median value of 0.64 R_\odot , and stellar masses span $M_s \in [0.13, 0.88] M_\odot$ with a median value of 0.67 M_\odot . Our final *Kepler* sample boasts a median fractional R_s uncertainty of $\sim 6.7\%$ which is ~ 4 –5 times smaller than the typical R_s uncertainty reported in the KSPC. The median fractional uncertainty on M_s is $\sim 5.5\%$.

2.2. *K2* stellar sample

We first retrieved the list of probable low mass dwarf stars observed in any *K2* campaign by querying MAST⁵. Our initial search was restricted to *K2* stars with $T_{\text{eff}} < 4900$ K, $\log g > 4$, and $R_s < 1 R_\odot$. Note that these criteria are not intended to represent the parameter ranges for low mass dwarf stars but are intended as conservative conditions to encapsulate all such stars prior to their refinement using the *Gaia* DR2 data. From MAST, we retrieve each star’s Ecliptic Plane Input Catalog (EPIC) numerical identifier, stellar photometry in the *Kepler* bandpass K_p and 2MASS bands JHK_s , along with measured values of T_{eff} , $\log g$, [Fe/H], and R_s .

We proceed with refining the stellar parameters by cross-matching our initial *K2* sample with *Gaia* DR2 using the *Gaia-K2* data products from Megan Bedell⁶.

⁵ Mikulski Archive for Space Telescopes, <https://archive.stsci.edu/k2/>.

⁶ <https://gaia-kepler.fun/>

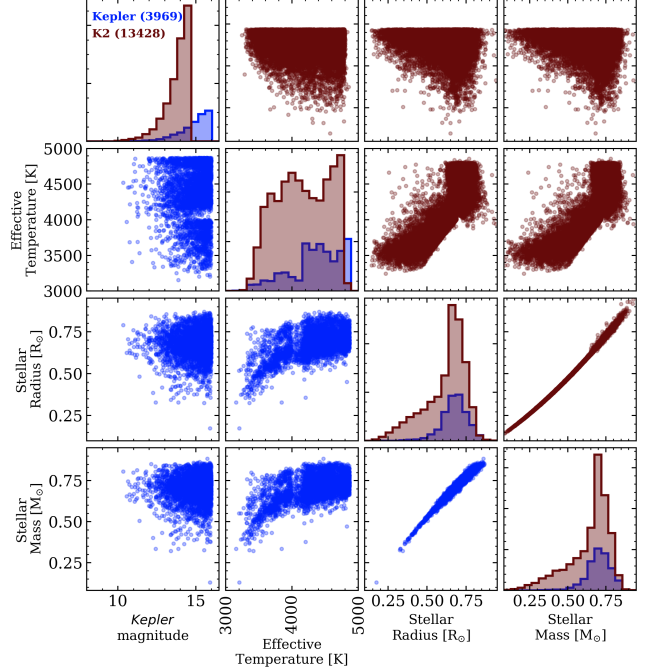


FIG. 2.— Low mass dwarf stellar samples from *Kepler* and *K2*. Distributions of *Kepler* magnitudes, effective temperatures, stellar radii, and stellar masses for stars in our final stellar sample from either *Kepler* (blue histogram and markers) or *K2* (red histogram and markers).

Where available, we retrieve each star’s celestial coordinates, stellar parallaxes ϖ , and *Gaia* photometry. Measurements of R_s then follow from the methodology of Berger et al. (2018) which is outlined as follows. The formalism of Bailer-Jones et al. (2018) is used to transform the assumed Gaussian-distributed ϖ PDFs into stellar distance PDFs which need not remain Gaussian. Using the measured distances d and celestial coordinates, we interpolate over the E_{B-V} extinction maps using the `mwdust` software (Bovy et al. 2016) to derive both the V and K_s -band extinction coefficients A_V and A_{K_s} . We then calculate each star’s absolute K_s -band magnitude $M_{K_s} = K_s - \mu - A_{K_s}$ where the distance modulus is $\mu = 5 \log_{10}(d/10 \text{ pc})$.

For the earliest stars in our sample ($M_{K_s} \leq 4.6$), for which the bolometric corrections are reliable, we interpolate the MIST bolometric correction grids (Choi et al. 2016) over T_{eff} , $\log g$, [Fe/H], and A_V to derive the K_s -band bolometric corrections BC_{K_s} . We then compute the absolute bolometric magnitudes $M_{\text{bol}} = M_{K_s} + BC_{K_s}$ and consequently the bolometric stellar luminosities from

$$L_{\text{bol}} = L_0 \cdot 10^{-0.4M_{\text{bol}}}, \quad (1)$$

where $L_0 = 3.0128 \times 10^{28}$ W (Mamajek et al. 2015). The refined R_s values are then calculated using the Stefan-Boltzmann law given L_{bol} and T_{eff} , with measurement uncertainties propagated throughout.

For the remaining late type stars with $M_{K_s} > 4.6$, we revert to the empirically-derived radius-luminosity relation from Mann et al. (2015) to calculate the M dwarf stellar radii. Mann et al. (2015) fit a second-order polynomial to R_s as a function of M_{K_s} which has a characteristic dispersion in the fractional radius uncertainty of 2.89%. To quantify the final R_s uncertainty we sample

M_{K_s} from its posterior PDF and transform each M_{K_s} draw to an R_s value using the aforementioned radius-luminosity relation. We then add, in quadrature, an additional dispersion term equal to the dispersion in the radius-luminosity relation. Stellar masses within our $K2$ sample are derived identically to the method applied to the *Kepler* sample using the Boyajian et al. (2012) stellar mass-radius relation (see Sect. 2.1).

We define our final $K2$ stellar sample of low mass dwarf stars similarly to our definition of the *Kepler* sample. Explicitly, we focus on stars that obey the following criteria:

1. $K_p < 14.7$,
2. $T_{\text{eff}} - \sigma_{T_{\text{eff}}} \leq 4700$ K,
3. $R_s - \sigma_{R_s} \leq 0.8 R_{\odot}$,
4. $M_s - \sigma_{M_s} \leq 0.8 M_{\odot}$, and
5. $R_s < R_{s,\text{max}}$.

Because our $K2$ sample lacks any evolutionary flags, we adopt the following ad hoc upper limit on R_s from Fulton et al. (2017) that aims to reject evolved stars:

$$R_{s,\text{max}} = R_{\odot} \cdot 10^{0.00025(T_{\text{eff}}/\text{K}-5500)+0.2}. \quad (2)$$

Based on these criteria, we retrieve 13428 low mass $K2$ stars whose stellar parameters are also depicted in Figure 2. In our $K2$ sample, the *Kepler* magnitudes span $K_p \in [8.47, 14.68]$ with a median value of 14.04, effective temperatures span $T_{\text{eff}} \in [3246, 4856]$ K with a median value of 4017 K, stellar radii span $R_s \in [0.14, 0.94] R_{\odot}$ with a median value of 0.66 R_{\odot} , and stellar masses span $M_s \in [0.09, 0.93] M_{\odot}$ with a median value of 0.65 M_{\odot} . The stars in this sample exhibit a median fractional R_s uncertainty of $\sim 3.5\%$ which is ~ 2 times smaller than the typical R_s uncertainty obtained for stars in our *Kepler* sample. The median fractional uncertainty on M_s is $\sim 3.9\%$.

Our full stellar sample therefore contains 17393 stars. Each of the *Kepler* and $K2$ stellar samples is dominated by mid-to-late K dwarfs with temperatures and radii $\gtrsim 3800$ K and $\gtrsim 0.6 R_{\odot}$ respectively. This fact will have important implications on our ability to precisely measure the planet occurrence rate around the lowest mass stars in our sample.

3. POPULATION OF SMALL CLOSE-IN PLANETS AROUND LOW MASS DWARF STARS

Here we define the population of small close-in planets orbiting stars contained in our stellar sample. Our initial sample of transiting planets from either *Kepler* or $K2$ were retrieved from the NASA Exoplanet Archive (Akeson et al. 2013) on June 15, 2019. Only confirmed planets—based on their Exoplanet Archive dispositions—with orbital periods $P \in [0.5, 100]$ days are included. By considering confirmed planets only, we naturally focus on the true empirical population of small close-in planets without being contaminated by astrophysical false positives that may plague the planet candidate sample that is excluded from our initial sample.

The refined stellar radii derived in Sect. 2 enable us to derive more precise planetary radii. We refine the planetary radii r_p by retrieving point estimates of each planet's

scaled planetary radius r_p/R_s , which often includes a median value accompanied by the 16th and 84th percentiles of the r_p/R_s posterior PDF. In cases for which the r_p/R_s uncertainties are symmetric, we assume that the r_p/R_s posterior PDF is Gaussian. For planets with asymmetric reported uncertainties, we fit the r_p/R_s percentiles with a skew-normal distribution using the `scipy.skewnorm` python class. We fit for the location, scale, and shape parameters of the distribution such that its resulting percentiles are consistent with the r_p/R_s point estimates reported for each planet. The refined planetary radii are then derived by sampling the product of the r_p/R_s and R_s distributions. Our planet sample is then updated by only considering planets whose radii are consistent with $r_p = 0.5 - 4 R_{\oplus}$.

From the distributions of R_s , T_{eff} , M_s , and P for each planet and host star, we derive the planets' semimajor axes a using Kepler's third law and insolations F from

$$\frac{F}{F_{\oplus}} = \left(\frac{R_s}{R_{\odot}} \right)^2 \left(\frac{T_{\text{eff}}}{5777 \text{ K}} \right)^4 \left(\frac{a}{1 \text{ AU}} \right)^{-2}. \quad (3)$$

Our final sample of confirmed small close-in planets contains 275 *Kepler* and 53 $K2$ planets respectively. Their respective median fractional radius uncertainties are 7.1% and 9.0%. Properties of the 328 confirmed planets in our sample are reported in Table 1 and Table 2. Our planet sample is depicted in Figure 3 as two-dimensional maps of the number of planet detections in the $P - r_p$ and $F - r_p$ spaces. The two-dimensional histogram maps are computed by Monte-Carlo sampling planets from their F and r_p measurement uncertainties and with a fractional precision on P inflated to 20%.

The empirical planet population in Figure 3 exhibits many recognizable features in the distribution of planets orbiting low mass stars (e.g. Morton & Swift 2014; Dressing & Charbonneau 2015; Gaidos et al. 2016). Namely, the dearth of planets with $r_p \gtrsim 2 R_{\oplus}$ at short orbital periods known as the Neptunian desert (Lundkvist et al. 2016; Mazeh et al. 2016), the prominence of super-Earth and sub-Neptune-sized planets with orbital periods of a few to tens of days, and the lack of small planets at long orbital periods ($P \gtrsim 40$ days) due to the poor transit detection completeness in this region. Any features resembling the radius valley are not prominent in the empirical planet distribution. Assuming that the radius valley around Sun-like stars persists in some form around low mass stars, the fact that a distinct valley is not visible in the empirical planet population highlights the importance of measuring valley features from the completeness-corrected planet distribution. Alternatively, the valley—close to the expected rocky to non-rocky transition of $\sim 1.5 - 1.8 R_{\oplus}$ (Weiss & Marcy 2014)—may not be entirely void of planets. Indeed there exists a significant subset of confirmed planets between 1.5-1.8 R_{\oplus} with periods out to ~ 12 days indicating that the mechanism responsible for producing the radius valley might not be as efficient as when operating on planetary systems around Sun-like stars.

4. TRANSITING PLANET DETECTION COMPLETENESS

Derivation of the planet occurrence rate requires the empirical distribution of planet detections to be corrected for imperfect survey completeness. The completeness

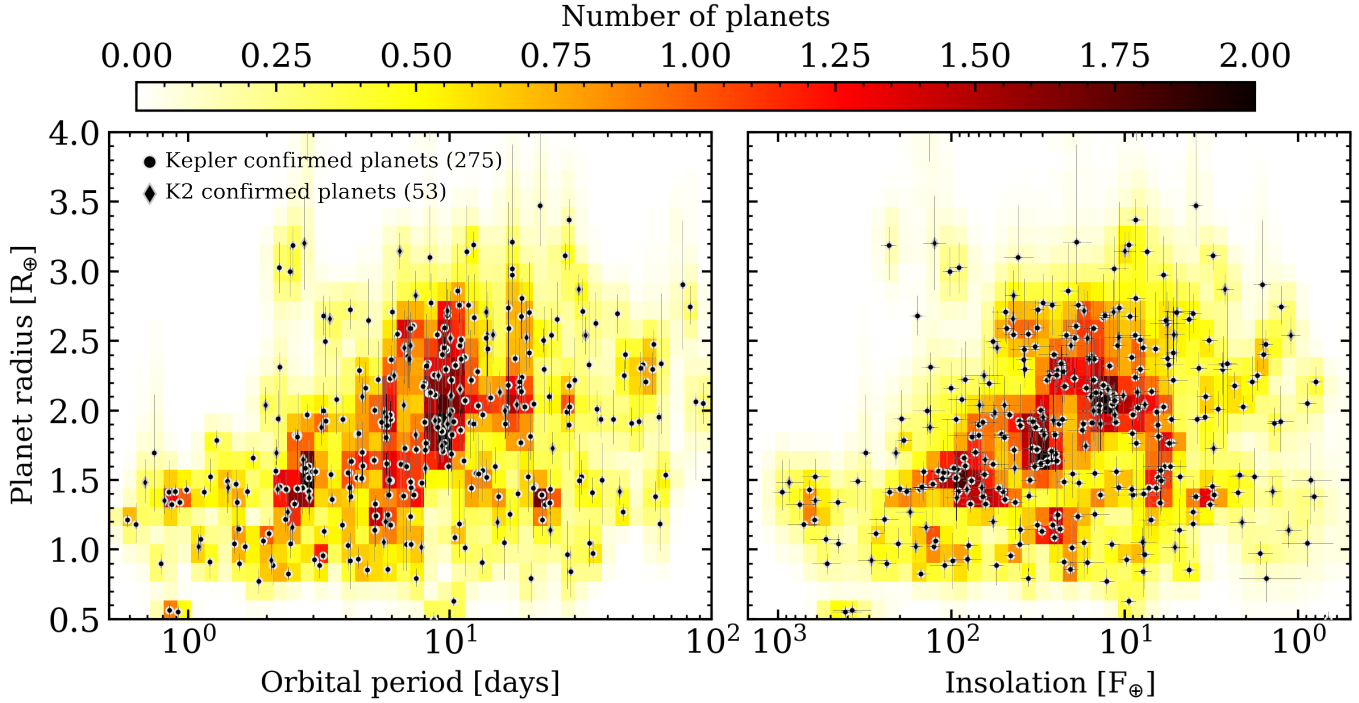


FIG. 3.— (*Interactive figure*) Empirical population of confirmed close-in planets around low mass stars. The distribution of 275 and 53 confirmed planets from *Kepler* and *K2* (circles and diamonds respectively) as a function of orbital period, insolation, and planet radius. The two-dimensional maps are Monte-Carlo sampled from the measurement uncertainties on the planetary radii and isolations while the fractional uncertainties on the orbital periods are inflated to 20%.

TABLE 1
KEPLER CONFIRMED PLANET PARAMETERS

| KIC | Planet name | P [days] | F [F_{\oplus}] | F upper limit [F_{\oplus}] | F lower limit [F_{\oplus}] | r_p [R_{\oplus}] | r_p upper limit [R_{\oplus}] | r_p lower limit [R_{\oplus}] |
|---------|---------------|---------------|-------------------------|-------------------------------------|-------------------------------------|---------------------------|---------------------------------------|---------------------------------------|
| 2556650 | Kepler-1124 b | 2.85235 | 46.5 | 4.7 | 4.6 | 1.97 | 0.08 | 0.10 |
| 2715135 | Kepler-753 b | 5.74771 | 40.2 | 4.6 | 4.5 | 1.89 | 0.30 | 0.12 |
| 3234598 | Kepler-383 b | 12.90468 | 20.2 | 2.8 | 2.5 | 1.54 | 0.30 | 0.17 |
| 3234598 | Kepler-383 c | 31.20122 | 6.2 | 0.8 | 0.8 | 1.49 | 0.34 | 0.22 |
| 3426367 | Kepler-1308 b | 2.10434 | 55.3 | 5.6 | 5.1 | 0.89 | 0.03 | 0.14 |

NOTE. — Only the first five rows are shown here to illustrate the table's content and format. The complete table in csv format is available in the arXiv source.

TABLE 2
K2 CONFIRMED PLANET PARAMETERS

| EPIC | Planet name | P [days] | F [F_{\oplus}] | F upper limit [F_{\oplus}] | F lower limit [F_{\oplus}] | r_p [R_{\oplus}] | r_p upper limit [R_{\oplus}] | r_p lower limit [R_{\oplus}] |
|-----------|-------------|---------------|-------------------------|-------------------------------------|-------------------------------------|---------------------------|---------------------------------------|---------------------------------------|
| 201110617 | K2-156 b | 0.81315 | 615.4 | 51.0 | 55.4 | 1.35 | 0.12 | 0.10 |
| 201155177 | K2-42 b | 6.68796 | 54.8 | 6.7 | 5.7 | 2.45 | 0.27 | 0.25 |
| 201205469 | K2-43 c | 2.19888 | 81.8 | 8.5 | 7.9 | 1.43 | 0.09 | 0.08 |
| 201205469 | K2-43 b | 3.47114 | 44.4 | 4.9 | 4.3 | 2.66 | 0.17 | 0.13 |
| 201208431 | K2-4 b | 10.00440 | 16.5 | 1.8 | 1.6 | 2.52 | 0.34 | 0.31 |

NOTE. — Only the first five rows are shown here to illustrate the table's content and format. The complete table in csv format is available in the arXiv source.

correction is treated separately for each subset of planets from *Kepler* or *K2* in the following subsections. Each set of corrections is designed to account for detection biases arising from the imperfect transit detection sensitivity and for the geometric probability of a planetary transit to occur.

4.1. *Kepler* sensitivity

The derivation of the *Kepler* planet detection sensitivity follows from the methodology outlined in Christiansen et al. (2016) and used by Fulton et al. (2017) to resolve the radius valley around FGK stars. Per-target *Kepler* completeness products for DR25 and the SOC 9.3 version of the *Kepler* pipeline (Jenkins et al. 2010) are available for all of the stars in our *Kepler* sample (Burke et al. 2015; Burke & Catanzarite 2017). Detection sensitivities (or efficiencies) were calculated via transiting planetary signal injections at the pixel level. The light curves with injected signals were subsequently processed by the *Kepler* pipeline Transiting Planet Search (TPS) module from which the detection sensitivity is computed as the fraction of injected signals that are successfully recovered by the pipeline as a function of the Multi-event statistic (MES; Christiansen et al. 2015, 2017).

The MES represents the level of significance of a repeating transit signal at a specified transit duration ranging from 1.5–15 hours. Following Petigura et al. (2018), we adopt an alternative diagnostic for the transit signal significance in the form of the transit signal-to-noise ratio

$$\text{S/N} = \frac{Z}{\text{CDPP}_D} \sqrt{n_{\text{transits}}(\mathbf{t}, P, T_0)} \quad (4)$$

where $Z = (r_p/R_s)^2$ is the transit depth assuming a non-grazing transit (i.e. $b \lesssim 0.9$), CDPP_D is the Combined Differential Photometric Precision on the timescale of the transit duration D (Koch et al. 2010), and n_{transits} is the number of observed transits given the target’s data span and duty cycle of the observations \mathbf{t} , the planet’s orbital period P , and its time of mid-transit T_0 .

To compute the *Kepler* detection sensitivity as a function of S/N, we first derive the mapping between the MES and the transit S/N using the data from Christiansen et al. (2015) who derived the detection sensitivity of the *Kepler* pipeline from one year of data. The parameters of the injected planets are provided along with their corresponding MES and CDPP at each value of D considered. For each injected planet, we interpolate its MES and CDPP values to D and calculate the corresponding transit S/N using Eq. 4. The mapping between MES and S/N is shown in Figure 4 for the full set of injected planets whose transit S/N values span 2.7–4843. Given the large number of injected planetary signals ($> 10^4$), we fit the number-weighted S/N to MES mapping using the `scipy.curve_fit` non-linear least squares algorithm with a powerlaw function of the form $\text{MES} = A \cdot \text{S/N}^\alpha$. We find a best-fit amplitude and powerlaw index of $A = 0.977$ and $\alpha = 0.967$ respectively with negligible uncertainties. This relation is used to map the transit S/N to MES which is then mapped to the detection sensitivity. The average detection sensitivity curve for stars in our *Kepler* sample, and as a function of transit S/N, is shown in Figure 5 along with its 16th and 84th percentiles.

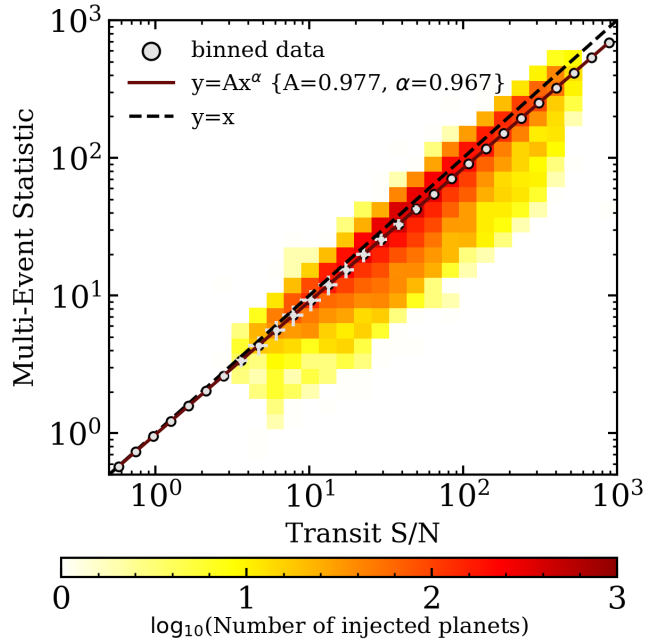


FIG. 4.— Correlation between the *Kepler* multi-event statistic and transit S/N. The mapping between the MES and S/N based on the synthetic planetary signals injected into the *Kepler* pipeline (Christiansen et al. 2015). The number-weighted powerlaw fit (solid line) to the correlation differs slightly from a one-to-one relation (dashed line) with a marginally lower amplitude and shallower slope.

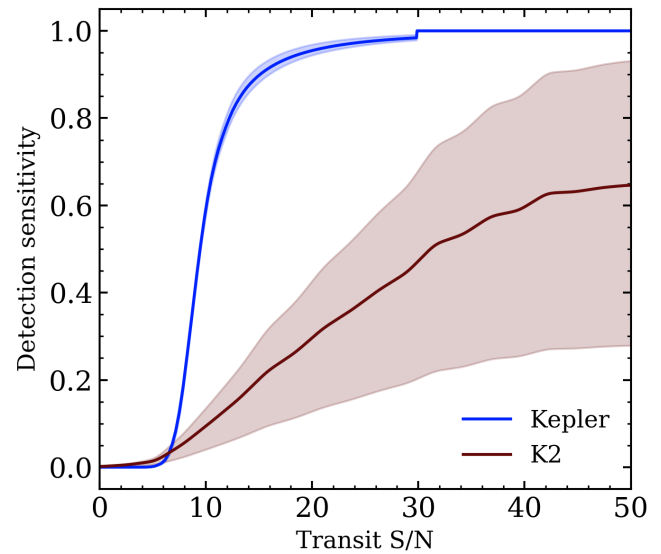


FIG. 5.— Average detection sensitivity for *Kepler* and *K2*. The solid curves represent the average transiting planet detection sensitivity for the *Kepler* and *K2* stars in our sample as a function of the transit S/N (Eq. 4). The shaded regions mark the 16th and 84th percentiles of the measured detection sensitivities.

4.2. *K2* sensitivity

Unlike the primary *Kepler* mission, the *K2* data products do not feature detailed completeness and reliability products. To derive the detection sensitivity among the *K2* stars in our sample we employ the transit detection pipeline ORION (Cloutier 2019).

The failure of the second reaction wheel on board the *Kepler* spacecraft in 2013 prevented the observatory

from maintaining the fine pointing accuracy required to continue to obtain ultra precise photometry. The repurposed *K2* mission exploited the solar wind pressure by enabling the observatory to continue pointing along the ecliptic plane with realignments via thruster firings (Howell et al. 2014). ORION does not feature a specialized module to correct for the temporally correlated pointing corrections. This requires that pointing-corrected light curves be used as input. We adopt the EVEREST-reduced *K2* light curves which use a pixel level decorrelation to remove systematics from the spacecraft’s variable pointing (Luger et al. 2016, 2018). We favor the EVEREST *K2* light curves over light curves produced by analogous pipelines (e.g. K2SFF; Vanderburg & Johnson 2014, K2SC; Aigrain et al. 2015, 2016) due to its demonstrated performance in obtaining improved photometric precision by a factor of $\sim 20 - 50\%$ (Luger et al. 2016).

We quantify the *K2* detection sensitivity using ORION by first retrieving the EVEREST light curve from MAST for each star in our sample. We only consider light curves from individual campaigns. As ORION input we supply the time sampling t in BJD, the corrected flux, and flux uncertainties in e⁻/second, from the EVEREST keywords TIME, FCOR, and FRAW_ERR. The duty cycle is derived by restricting to light curve measurements for which the QUALITY flag is zero. In light curves with known signals from planets or planet candidates, those signals are modeled and removed from the light curve based on their reported transit parameters and using the batman (Kreidberg 2015) implementation of the Mandel & Agol (2002) transit model. We then inject transiting planetary signals directly into the light curve by sampling planets from the linear transit S/N grid $\mathcal{U}(0, 50)$. The per-system multiplicity is drawn from the cumulative occurrence rate of small planets out to 200 days around mid-K to early M dwarfs from *Kepler* (2.5 ± 0.2 ; Dressing & Charbonneau 2015). Each planet’s time of mid-transit T_0 is drawn from $\mathcal{U}(\min(t), \max(t))$. In a given light curve, with fixed t and CDPP_D, for a star whose R_s and M_s values are fixed to their maximum likelihood values, we draw each planet’s logarithmic orbital period from $\mathcal{U}(\log_{10}(0.5 \text{ days}), \log_{10}(200 \text{ days}))$ which allows us to compute the number of transits that occur within t . Note that some injected planets will exhibit $n_{\text{transits}} = 0$ due to the limited *K2* baselines of typically ~ 80 days. The drawn orbital period also uniquely determines the planet’s radius corresponding to its drawn value of the S/N. To ensure dynamical stability in multi-planet systems, we compute the maximum likelihood planet mass from the probabilistic mass-radius relation forecaster (Chen & Kipping 2017) and analytically assess the Lagrange stability of each neighboring planet pair assuming circular orbits (Barnes & Greenberg 2006). Each planet’s scaled semimajor axis a/R_s and scaled radius r_p/R_s follow from their sampled radius r_p and the stellar parameters R_s and M_s . We sample impact parameters b from $\mathcal{U}(0, 0.9)$ to compute the orbital inclinations. Furthermore, we adopt fixed quadratic limb darkening coefficients by interpolating the *Kepler* bandpass coefficient grid along T_{eff} , $\log g$, and [Fe/H], assuming solar metallicity when [Fe/H] measurements are absent (Claret et al. 2012). These parameters are used to compute transit models in the absence of any transit timing variations. Transit signals are then injected into the cleaned *K2* light

curves and fed to ORION to conduct a blind search for transiting signals.

The detection sensitivity as a function of S/N for each *K2* star is computed by considering 10^2 injected planetary systems per star and computing the recovery fraction of injected planets with $P \leq 100$ days. The average *K2* detection sensitivity curve, along with the 16th and 84th percentiles, are also included in Figure 5. The quality of the pointing corrections within the EVEREST light curves can vary widely within our sample such that there is considerably more variance in the *K2* detection sensitivity relative to *Kepler*. Furthermore, the maximum detection sensitivity is seen to be approximately 60-70% that of *Kepler*, a result that is consistent with recent investigations of the completeness in *K2* Campaign 5 (Zink et al. 2020). The reduced sensitivity is due in-part to the imperfect corrections of the pointing and to the lesser time baseline of ~ 80 days in a typical *K2* light curve compared to *Kepler*. Furthermore, ORION was originally developed for use on the 2-minute cadence data from the *TESS* mission. Here we have not attempted to optimize the performance of ORION on *K2* light curves beyond slight modifications to the algorithm’s performance hyperparameters that were made to ensure the detection of 52/53 confirmed *K2* planets. The planet K2-21c (EPIC 206011691.02, $P = 15.5$ days) remains undetected by ORION because of the algorithm’s requirement to discard putative signals that are commensurate with other high S/N signals in the light curve. The presence of K2-21b at $P = 9.32$ days is within 1% of a 5:3 period ratio with K2-21c and thus prohibits the identification of the 15.5 day signal as being independent and planetary.

4.3. Two-dimensional sensitivity maps

The sensitivity curves depicted in Figure 5 enable us to extend the visualization of the detection sensitivity to two dimensions. Explicitly, we consider the detection sensitivity s_{nij} for each star (indexed by n) and as a function of P and r_p which are indexed by i and j respectively. The calculation of the sensitivity in $P - r_p$ space is needed to evaluate the occurrence rates in that parameter space. Resolving the structure of the radius valley in $P - r_p$ space is required to understand the efficiency of atmospheric loss on both planet size and separation regardless of the physical mechanism responsible.

We consider orbital periods $P \in [0.5, 100]$ days and planet radii $r_p \in [0.5, 4] R_\oplus$. For each star n , and at each grid cell ij , we compute the average S/N. This value is then mapped to the detection sensitivity of that grid cell using the curves in Figure 5. The resulting detection sensitivity maps for *Kepler* and *K2*, averaged over n , are shown in Figure 6.

4.4. Survey completeness

Only transiting planets are detectable in transit surveys. To correct for the non-detection of otherwise detectable but non-transiting planets, we compute the geometric transit probability p_t for each star n and at each grid cell ij in the $P - r_p$ space to be

$$p_{t,nij} = \frac{R_{s,n}}{a_{ni}}. \quad (5)$$

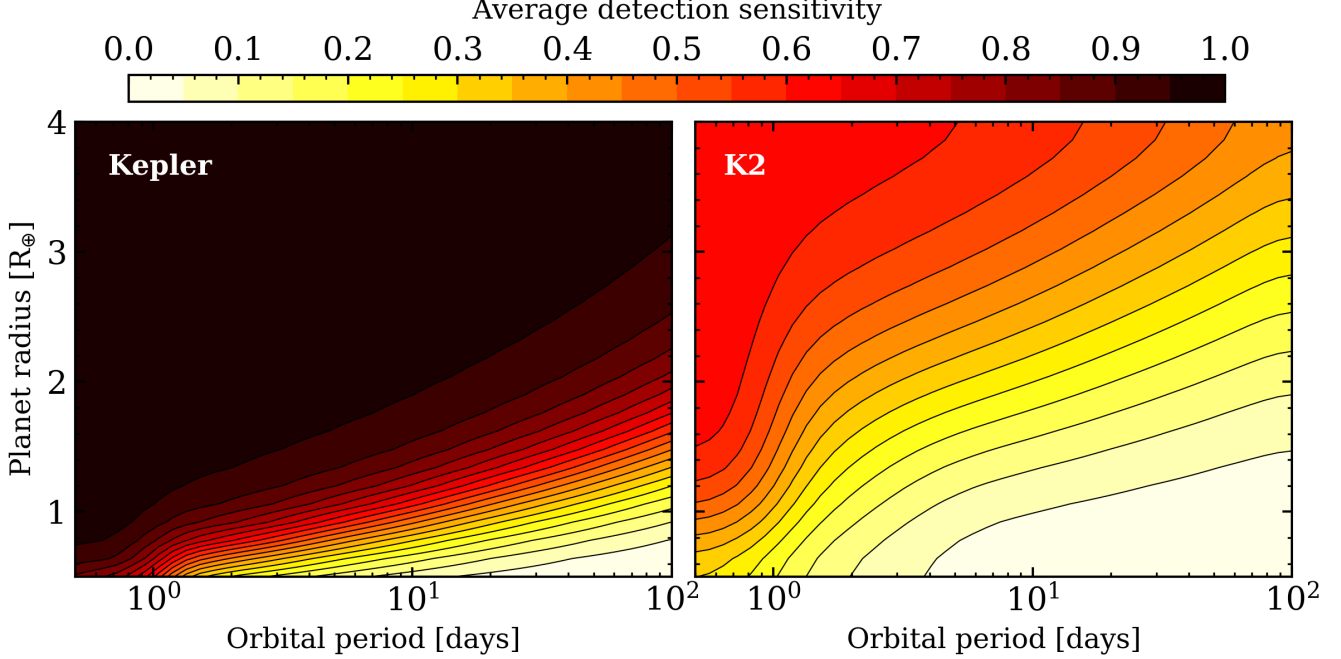


FIG. 6.— Average detection sensitivity versus orbital period and planetary radius. The detection sensitivity maps averaged over *Kepler* stars (left panel) and over *K2* stars (right panel) from our sample of low mass dwarf stars.

Note that we are only interested in the relative planet occurrence rate and therefore do not consider constant scalar modifications to $p_{t,nij}$ from effects such as grazing transits or non-zero eccentricities (Barnes 2007).

The product of each star’s detection sensitivity with its geometric transit probability yield completeness maps as a function of P and r_p . The average completeness maps for our *Kepler* and *K2* stars are shown in Figure 7.

5. THE OCCURRENCE RATE OF SMALL CLOSE-IN PLANETS AROUND LOW MASS DWARF STARS

5.1. Occurrence rates versus orbital period and planet radius

The detection and validation of planets from the *Kepler* and *K2* missions enables the measurement of the occurrence rate of planets given the completeness corrections derived in Sect. 4. For the index i representing a planet’s orbital period and j representing the planetary radius, the probability of detecting an integer number of planets within that grid cell (k_{ij}), around N_s stars, is given by the binomial likelihood function

$$\mathcal{L}_{nij}(k_{ij}|N_s, P_{nij}) = \binom{N_s}{k_{ij}} \prod_{n=1}^{N_s} P_{nij}^{k_{ij}} (1 - P_{nij})^{N_s - k_{ij}} \quad (6)$$

where

$$P_{nij} = s_{nij} \cdot p_{t,nij} \cdot f_{ij}, \quad (7)$$

is the probability of detecting a planet in the ij grid cell around the n^{th} star. This quantity is dependent on the detection sensitivity s_{nij} , the transit probability $p_{t,nij}$, and the intrinsic occurrence rate of planets in the grid cell f_{ij} , which is assumed to be universal among all N_s stars in the sample. Recall that the number of planet detections k_{ij} was depicted in Figure 3 and calculations of s_{nij} and $p_{t,nij}$ produced the completeness maps shown

in Figure 7. Taken together, and noting from Bayes theorem that the posterior probability of f_{ij} is

$$p(f_{ij}|N_s, s_{nij}, p_{t,nij}, k_{ij}) \propto \mathcal{L}_{nij}(k_{ij}|N_s, s_{nij}, p_{t,nij}, f_{ij}), \quad (8)$$

modulo the coefficient of proportionality which we set to unity, we are able to compute the maximum a-posteriori (MAP) occurrence rate and uncertainty maps according to Eq. 8.

Before proceeding, first recall that our planet sample contains ~ 5 times more confirmed planets from *Kepler* than from *K2* (see Figure 3) despite our stellar sample containing ~ 4.4 times more stars observed by *K2* than by *Kepler* (see Figure 2). These factors compound to produce a lower planet occurrence rate measured from *K2* confirmed planets than with *Kepler* as the reduced *K2* detection completeness (see Figure 7) is insufficient to account for the lower measured planet occurrence rates. Explicitly, we measure cumulative occurrence rates of 2.48 ± 0.32 and 0.75 ± 0.11 confirmed planets per star with $P \in [0.5, 100]$ days and $r_p \in [0.5, 4] R_\oplus$ from *Kepler* and *K2* respectively. The discrepancy arises from the disparate resources that have been dedicated to the validation of planet candidates from *Kepler* and *K2*. The result being that the number of real planets within the full set of *K2* planet candidates is underestimated by the number of planet candidates that have been reported as validated to date. We address this discrepancy by scaling the cumulative occurrence rate measured by *K2* to that of *Kepler*. In this way, we are implicitly assuming that the planet populations studied by each mission are inherently equivalent, despite existing around distinct stellar populations within the galaxy, albeit with similar physical properties. In Sect. 5.4 we will revisit the comparison of the planet occurrences rates from *Kepler* and *K2* following the inclusion of *K2* planet candidates.

The MAP f_{ij} map is depicted in Figure 8. Here, the

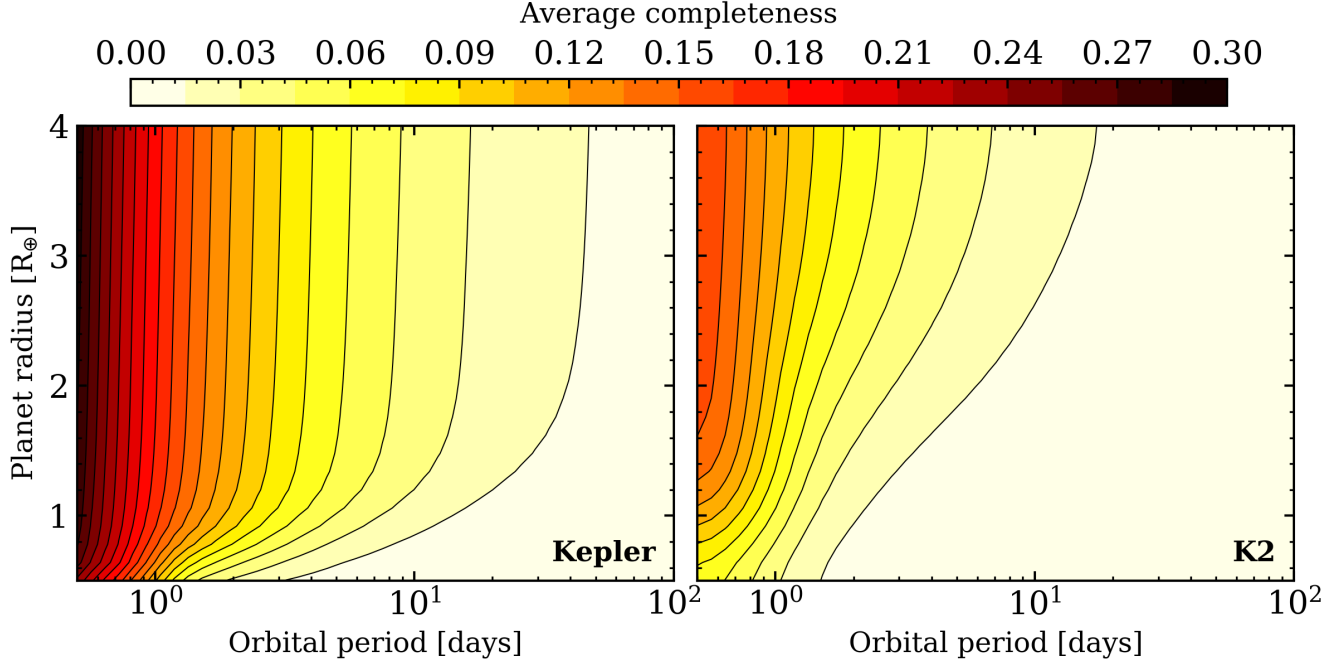


FIG. 7.— Average completeness versus orbital period and planetary radius. Maps of the product of the detection sensitivity and geometric transit probability averaged over *Kepler* stars (left panel) and over *K2* stars (right panel) from our sample of low mass dwarf stars.

existence of the radius valley around low mass stars is clearly evident. Distinct peaks in the planet frequency are separated along the planetary radius axis and span $\sim 0.9\text{--}1.4 R_{\oplus}$ and $\sim 1.9\text{--}2.3 R_{\oplus}$ respectively. Note however that the lower limit on the former peak approaches the region in which the *Kepler* sensitivity falls below 10% and the f values become unreliable. The occurrence rates also highlight the relative dearth of planets larger than $\sim 3 R_{\oplus}$ including the Neptunian desert at short orbital periods (Lundkvist et al. 2016; Mazeh et al. 2016). The large scale structure of the measured occurrence rates are also broadly consistent with previous investigations of the planet population around low mass *Kepler* stars (Morton & Swift 2014; Dressing & Charbonneau 2015; Gaidos et al. 2016) such as the prominence of planets $\lesssim 2 R_{\oplus}$ with $P \sim 10\text{--}60$ days and the measured cumulative occurrence rate of 2.48 ± 0.32 planets per star with $P \in [0.5, 100]$ days and $r_p \in [0.5, 4] R_{\oplus}$.

The location and slope of the radius valley (i.e. $dr_p/d\log P$) appear broadly consistent with the valley structure measured from the empirical planet population of FGK stars characterized via asteroseismology (Van Eylen et al. 2018). Wu (2019) also provided a visual approximation to the location of the radius valley around stars with $M_s \in [0.5, 0.76] M_{\odot}$ in their *Gaia*-*Kepler* sample. However, we find the location of the terrestrial-sized planet peak to exist at longer $P \sim 30$ days compared its location at ~ 5 days from Wu (2019) (c.f. Figure 2). The discrepancy likely originates from differences in the method of correcting for survey incompleteness. Recall that in this study the detection sensitivity for *Kepler* stars is computed on a per star basis given the unique completeness products from the *Kepler* pipeline whereas Wu (2019) adopt the piecewise completeness levels of 10, 50, or 90% complete as a function of P and r_p from Zhu et al. (2018).

Also included in Figure 8, are planets with $\geq 3\sigma$ bulk

density measurements (ρ_p) from either precision radial velocities or transit timing variations. Planet parameters are retrieved from the NASA Exoplanet Archive for planets orbiting stars with $T_{\text{eff}} \in [2800, 4700]$ K, whose orbital periods and radii span the domain considered in Figure 8, and whose masses are inconsistent with zero (i.e. no mass upper limits). The properties of the resulting 20 planets are listed in Table 3. Based on the planetary masses, radii, and compositional mass-radius relations from Zeng & Sasselov (2013), we define the following composition dispositions: *rocky* planets have bulk densities that are greater than or consistent with a purely rocky composition (i.e. 100% MgSiO₃) given the planet's size, *gaseous* planets have bulk densities that are less dense than and inconsistent with that of a pure water world (i.e. 100% H₂O) given the planet's size, and all remaining planets are flagged as having an *intermediate* bulk composition (i.e. not clearly terrestrial-like or likely to be hosting a significant H/He envelope).

The retrieved planets in Figure 8 demonstrate clear compositional clustering with planet radius. All rocky planets appear to be smaller than $1.8 R_{\oplus}$, independently of orbital period. Similarly, all four gaseous planets are larger than $2.6 R_{\oplus}$ while the three remaining planets with intermediate radii correspond to those with intermediate bulk compositions. Thus, we are justified in classifying the occurrence rate peak spanning $\sim 0.9\text{--}1.4 R_{\oplus}$ as representing rocky planets. The second peak between $\sim 1.9\text{--}2.3 R_{\oplus}$ hosts planets with intermediate bulk compositions that are clearly inconsistent with being rocky. However, due to degeneracies in planetary internal structure models, these planets are not unambiguously known to host extended H/He envelopes as their masses and radii are consistent with either being volatile-rich, or with having an Earth-like solid core plus an extended H/He envelope (Valencia et al. 2013). We

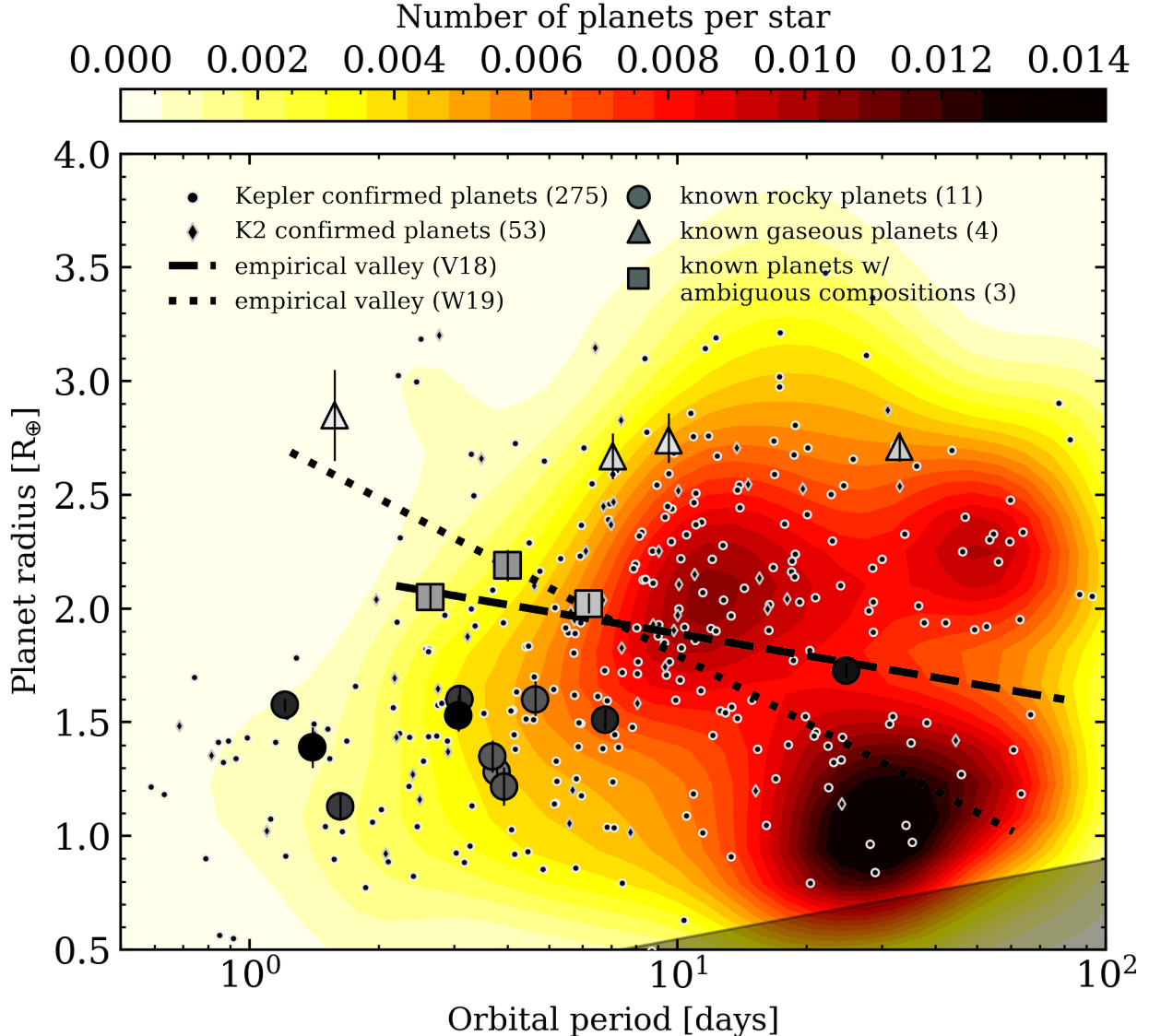


FIG. 8.— (Interactive figure) Planet occurrence rate versus orbital period and planetary radius. The maximum a-posteriori occurrence rate map calculated from the population of confirmed planets from *Kepler* and *K2* around low mass dwarf stars [small circles and diamonds]. For comparison, overplotted are the [dashed/dotted blue] empirical locations of the radius valley around FGK stars characterized via asteroseismology (dashed line, Van Eylen et al. 2018) and the approximate radius valley around mid-K to early-M dwarfs (dotted line, Wu 2019). Also overplotted are [blue] planets with $\geq 3\sigma$ bulk density measurements from the literature that are classified as having either a rocky (circles), a gaseous (triangles), or an intermediate (squares) bulk composition. Marker colors are indicative of the MAP planet bulk densities. The shaded region indicates where the *Kepler* sensitivity falls below 10%.

will refer to this peak in the occurrence rate distribution as the non-rocky peak in what follows.

To test the statistical significance of the bimodality in Figure 8, we used the `sklearn.mixture` package to fit the f_{ij} distribution with a Gaussian mixture model with 1-5 components. For the purpose of model comparison, we then computed the Bayesian Information Criterion (BIC) for each mixture model with its unique number of components. Multiple components are strongly favored over a single component indicating that the peaks in the occurrence rate distribution are significant. For example, $\Delta(\text{BIC}_{12}) = \text{BIC}_1 - \text{BIC}_2 \sim 400$ such that the two-component model is strongly fa-

vored over a single component⁷. We note that the three-component model is found to have the lowest BIC with $\Delta(\text{BIC}_{23}) = \text{BIC}_2 - \text{BIC}_3 \sim 90$ and $\Delta(\text{BIC}_{34}) = \text{BIC}_3 - \text{BIC}_4 \sim -10$ such that it is strongly favored over two components but only marginally favored over a more complex mixture model of four Gaussian components. The three components in the MAP f_{ij} map encapsulate the rocky planet peak plus the two apparent peaks around $\sim 2.2 R_\oplus$ and centered on ~ 11 days and ~ 50 days. Given the uncertainties on f_{ij} , which

⁷ Kass & Raftery (1995) recommend that a model n is strongly favored over a competing model m when $\Delta(\text{BIC}_{mn}) = \text{BIC}_m - \text{BIC}_n > 10$.

TABLE 3
PLANETS WITH $\geq 3\sigma$ BULK DENSITY MEASUREMENTS AROUND LOW MASS STARS

| Planet name | P [days] | F [F_{\oplus}] | r_p [R_{\oplus}] | m_p [M_{\oplus}] | ρ_p [g cm^{-3}] | Composition disposition | Refs. |
|-------------|------------|----------------------|------------------------|------------------------|---------------------------------|-------------------------|-------|
| GJ 357b | 3.93072 | 13.2 ± 1.4 | 1.22 ± 0.08 | 1.84 ± 0.31 | $5.67^{+1.75}_{-1.35}$ | Rocky | 1 |
| GJ 1132b | 1.62892 | 19.4 ± 4.0 | 1.13 ± 0.06 | 1.66 ± 0.23 | $6.39^{+1.36}_{-1.30}$ | Rocky | 2,3 |
| GJ 1214b | 1.58040 | 22.2 ± 3.0 | 2.85 ± 0.20 | 6.26 ± 0.86 | $1.50^{+0.44}_{-0.34}$ | Gaseous | 4 |
| GJ 9827b | 1.20898 | 326.9 ± 16.3 | 1.58 ± 0.03 | 4.91 ± 0.49 | $6.95^{+0.81}_{-0.71}$ | Rocky | 5 |
| GJ 9827c | 6.20147 | 37.0 ± 1.8 | 2.02 ± 0.05 | 4.04 ± 0.84 | $2.71^{+0.57}_{-0.55}$ | Intermediate | 5 |
| HD 219134b | 3.09293 | 176.7 ± 5.5 | 1.60 ± 0.06 | 4.74 ± 0.19 | $6.40^{+0.75}_{-0.69}$ | Rocky | 6 |
| HD 219134c | 6.76458 | 62.3 ± 1.9 | 1.51 ± 0.05 | 4.36 ± 0.22 | $7.01^{+0.83}_{-0.71}$ | Rocky | 6 |
| K2-18b | 32.93962 | 1.2 ± 0.1 | 2.71 ± 0.07 | 8.63 ± 1.35 | $2.40^{+0.41}_{-0.40}$ | Gaseous | 7,8 |
| K2-146b | 2.64460 | 19.2 ± 2.0 | 2.05 ± 0.06 | 5.77 ± 0.18 | $3.72^{+0.34}_{-0.30}$ | Intermediate | 9 |
| K2-146c | 4.00498 | 11.0 ± 1.1 | 2.19 ± 0.07 | 7.49 ± 0.24 | $3.96^{+0.38}_{-0.38}$ | Intermediate | 9 |
| Kepler-80b | 7.05246 | 41.8 ± 4.8 | 2.67 ± 0.10 | 6.93 ± 0.70 | $2.02^{+0.43}_{-0.35}$ | Gaseous | 10 |
| Kepler-80c | 9.52355 | 28.0 ± 3.2 | 2.74 ± 0.12 | 6.74 ± 0.86 | $1.82^{+0.45}_{-0.39}$ | Gaseous | 10 |
| Kepler-80d | 3.07222 | 126.5 ± 14.5 | 1.53 ± 0.09 | 6.75 ± 0.51 | $10.46^{+2.30}_{-2.04}$ | Rocky | 10 |
| Kepler-80e | 4.64489 | 72.9 ± 8.3 | 1.60 ± 0.08 | 4.13 ± 0.95 | $5.60^{+1.54}_{-1.32}$ | Rocky | 10 |
| L 98-59c | 3.69040 | 11.9 ± 1.5 | 1.35 ± 0.07 | 2.46 ± 0.31 | $5.55^{+1.32}_{-1.01}$ | Rocky | 11,12 |
| L 168-9b | 1.40150 | 144.2 ± 12.0 | 1.39 ± 0.09 | 4.60 ± 0.60 | $9.51^{+2.53}_{-2.11}$ | Rocky | 13 |
| LHS 1140b | 24.73696 | 0.5 ± 0.0 | 1.73 ± 0.03 | 6.98 ± 0.89 | $7.52^{+1.11}_{-1.06}$ | Rocky | 14 |
| LHS 1140c | 3.77793 | 6.1 ± 0.5 | 1.28 ± 0.02 | 1.81 ± 0.39 | $4.77^{+1.03}_{-1.01}$ | Rocky | 15 |
| LTT 3780b | 0.76845 | 106 ± 20 | 1.33 ± 0.08 | 3.12 ± 0.55 | $7.33^{+1.96}_{-1.64}$ | Rocky | 16 |
| LTT 3780c | 12.25205 | 2.63 ± 0.5 | 2.30 ± 0.16 | 8.50 ± 1.65 | $3.88^{+1.19}_{-1.03}$ | Intermediate | 16 |

NOTE. — References: 1) Luque et al. 2019 2) Dittmann et al. 2017a 3) Bonfils et al. 2018 4) Harpsøe et al. 2013 5) Rice et al. 2019 6) Gillon et al. 2017 7) Benneke et al. 2017 8) Cloutier et al. 2019b 9) Hamann et al. 2019 10) MacDonald et al. 2016 11) Kostov et al. 2019 12) Cloutier et al. 2019a 13) Astudillo-Defru et al. 2020 14) Dittmann et al. 2017b 15) Ment et al. 2019 16) ?.

are not communicated in Figure 8, it is unclear whether the third component at $P = 50\text{days}$ and $r_p = 2.2 R_{\oplus}$ is a real feature in the occurrence rate distribution. Deeper transiting planet searches around low mass stars will be required to investigate the validity of this third component.

Lastly, we note that the radius valley as a function of P is not completely void of planets. This may allude to the relative efficiencies of various gap clearing mechanisms around low mass stars and are discussed further in Sect. 7.3.

5.2. Occurrence rates versus planet radius

Next, we marginalize over P and compute the one-dimensional occurrence rate of small close-in planets as a function of r_p . The resulting occurrence rates are shown in Figure 9 in which the bimodal distribution of planet sizes is again clearly discernible in the MAP occurrence rates. The uncertainty on each f_j bin is computed from the 16th and 84th percentiles of its f_j posterior and are thus correlated given the smooth nature of the two-dimensional occurrence rates (Figure 8). In Figure 9 we ignore the measured occurrence rates in bins with $r_p \lesssim 1 R_{\oplus}$ where the detection sensitivity is poor.

From the bimodal distribution, we highlight the approximate radii likely corresponding to planets with rocky bulk compositions ($r_p \lesssim 1.54 R_{\oplus}$) versus planets with significant size fractions in an extended gaseous envelope ($r_p \gtrsim 1.54 R_{\oplus}$). A second depiction of f_j is included in Figure 9 with a bin width that is half that of

the principal f_j depiction (i.e. $0.06 R_{\oplus}$ compared to $0.13 R_{\oplus}$). With the finer binning, the fractional uncertainties on f_j are sufficiently large to eliminate the significance of the distinct bimodal peaks. Despite this, the bimodality in the MAP occurrence rate continues to persist with the location of the valley features only being marginally affected. We interpret this as further evidence for the existence of the radius valley in the close-in planet population around low mass stars.

Similarly to the two-dimensional occurrence rates in Sect. 5.1, we test the statistical significance of the apparent bimodality in Figure 9 by comparing the BIC values for 1-5 components of a Gaussian mixture model. We find that the two-component model has the lowest BIC and is strongly favored over a single component as $\Delta(\text{BIC}_{12}) = \text{BIC}_1 - \text{BIC}_2 \sim 20$. Furthermore, $\Delta(\text{BIC}_{23}) = \text{BIC}_2 - \text{BIC}_3 \sim -10$ such that two components are also favored over a more complex mixture model of three Gaussian components. These results emphasize that the detection of the valley is significant and that it likely features two components representing rocky and larger, non-rocky planet populations respectively.

5.3. Inclusion of supplemental K2 planet candidates

In an attempt to improve the counting statistics of the occurrence rate calculations, and to mitigate any bias introduced by solely focusing on confirmed planets, here we consider an enlarged planet sample that includes planet candidates (PCs). This new sample is the union of our existing sample of confirmed planets with a set of ad-

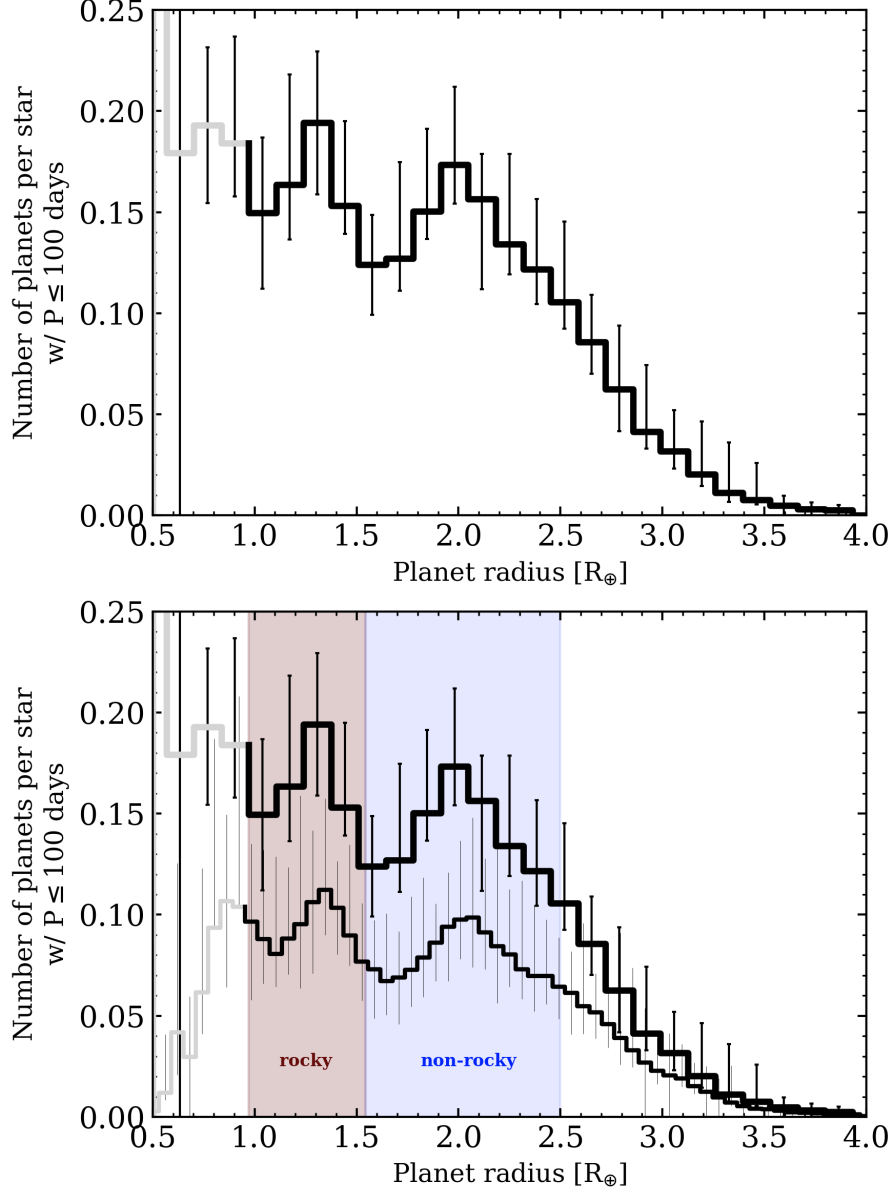


FIG. 9.— Occurrence rate of planets as a function of size. *Upper panel:* histogram depicting the relative occurrence rate of close-in planets with orbital periods < 100 days derived from the population of confirmed *Kepler* and *K2* planets around low mass stars. The bimodal distribution of planet radii peaking at occurrence rate-weighted radii of 1.12 and 2.07 R_{\oplus} indicates the presence of the radius valley around low mass stars centered at 1.54 R_{\oplus} . Uncertainties in the planet occurrences follow from binomial statistics and are limited by the relatively small number of confirmed planets around low mass stars from *Kepler* and *K2*. The measured occurrence rates below ~ 1 R_{\oplus} (shown in grey) should be ignored due to poor detection sensitivity. *Lower panel:* identical occurrence rates as in the upper panel accompanied by the same occurrence rates but with finer radius bins. The corresponding occurrence rate uncertainties per bin are inflated but the bimodal structure continues to be exhibited in the MAP occurrence rates. The shaded regions highlight our approximate definitions of rocky planets ($r_p \in [0.97, 1.54]$ R_{\oplus}), down to reasonable sensitivity limits, and non-rocky planets ($r_p > 1.54$ R_{\oplus}) around low mass stars. Note the 2.5 R_{\oplus} outer limit of the shaded region is chosen arbitrarily.

ditional PCs from the *K2* mission. Specifically, we consider the set of PCs reported by Kruse et al. (2019) from *K2* campaigns 0–8. This set includes 126 PCs that are not already included in our sample of confirmed planets but do orbit stars within our stellar sample.

By definition, we cannot identify which PCs are true planets of interest for this study and which PCs are instead produced by an astrophysical false positive. The inclusion of *K2* PCs therefore requires that we account for sample contamination by false positives probabilisti-

cally. We do so by considering six studies from the literature that perform a transiting planet search in *K2*—from any subset of its campaigns—and attempt to validate their uncovered PCs statistically based on follow-up observations (Montet et al. 2015; Crossfield et al. 2016; Dressing et al. 2017; Hirano et al. 2018; Livingston et al. 2018; Mayo et al. 2018). Each of these studies utilized some combination of ground-based photometry to validate planet ephemerides, reconnaissance spectroscopy to identify spectroscopic binaries, and speckle or AO-assisted imaging to search for nearby stellar companions.

TABLE 4
 $K2$ FALSE POSITIVE RATES FOR SMALL PLANETS AROUND COOL STARS

| Reference | N_{FP} | N_{VP} | FP rate [%] |
|---------------------------------------|-----------------|-----------------|----------------------|
| Montet et al. (2015) ^a | 0 | 8 | < 30.7 |
| Crossfield et al. (2016) | 2 | 39 | $4.9^{+6.0}_{-1.4}$ |
| Dressing et al. (2017) | 2 | 34 | $5.6^{+6.4}_{-2.0}$ |
| Hirano et al. (2018) ^a | 0 | 16 | < 19.5 |
| Livingston et al. (2018) ^a | 0 | 14 | < 21.0 |
| Mayo et al. (2018) ^b | 1 | 14 | $6.7^{+12.4}_{-2.0}$ |

NOTE. — Within each study we only consider PCs with $r_p < 4 \text{ R}_\oplus$ and orbiting cool stars with $T_{\text{eff}} < 4700 \text{ K}$. FP: false positive. VP: validated planet.

^a These studies do not detect any FPs such that the reported FP rate upper limit is represented by its 95% confidence interval.

^b Mayo et al. (2018) did not explicitly classify their non-validated planets as FPs so we define FPs within their sample as any PC whose false positive probability exceeds 10%.

Each of the aforementioned studies used their respective set of follow-up observations together with the statistical validation tool `vespa` (Morton 2012, 2015) to statistically classify their PCs as either a validated planet (VP)⁸, a false positive (FP), or some other inconclusive disposition (e.g. remains a PC). The FP rate around cool stars ($T_{\text{eff}} < 4700 \text{ K}$) from each study is estimated by calculating the ratio of the number of reported FPs to the total number of FPs plus VPs. Notably, Crossfield et al. (2016) showed that the FP rate in their $K2$ sample is dependent on the measured planet radius as giant PCs have a higher likelihood of being a FP. We therefore only focus on PCs with $r_p < 4 \text{ R}_\oplus$ when deriving FP rates.

The resulting FP rates are reported in Table 4. Half of the studies do not find any probable FP signals among the small PCs orbiting cool stars in their samples. In such cases, only upper limits on the FP rate can be derived which all agree that the FP rate is $\lesssim 20\%$ at 95% confidence. The remaining studies each detect at least one FP such that a non-zero maximum likelihood FP rate is measured. Their average FP rate is 5.7% which is also in agreement with the derived upper limits from the aforementioned studies.

We proceed by constructing 10^3 planet population realizations. Each realization includes all confirmed planets from both *Kepler* and $K2$, plus a subset of the 126 $K2$ PCs from Kruse et al. (2019). The subset of included PCs are randomly sampled from the full set of PCs according to the adopted FP rate such that each realization contains $(1 - 0.057) \cdot 126 \approx 119$ PCs. The effect of including PCs on the derived occurrence rates is assessed by comparing the f_j distributions measured with and without the inclusion of PCs in Figure 10. The radius valley continues to be resolved in the MAP occurrence rates. Furthermore, the addition of PCs reduces the median f_j uncertainty among planets with $r_p > 1 \text{ R}_\oplus$ from 0.0216 to 0.0186 planets per star (i.e. $\sim 15\%$ improvement). However, the partial filling of the gap is further sub-

stantiated as the contrast between the maximum f_j of the rocky planet peak ($r_p \sim 1.3 \text{ R}_\oplus$) and the minimum f_j of the valley ($r_p \sim 1.6 \text{ R}_\oplus$) decreases from 0.070 to 0.054 R_\oplus . This corresponds to a less significant detection of the bimodality in the radius valley as we find that $\Delta(\text{BIC}_{12}) \sim 4$ which is less than the value obtained when only confirmed planets are considered: $\Delta(\text{BIC}_{12}) \sim 20$. Contamination by true FPs in the planet sample containing PCs may contribute to the reduced significance of the valley so we revert to considering confirmed planets only for the remainder of this study.

5.4. Comparison of the recovered planet occurrence rates from *Kepler* and $K2$

Here we present a broad comparison of the occurrence rates of small close-in planets around low mass dwarf stars from *Kepler* and $K2$. Recall from Sect. 5.1 that we measure cumulative occurrence rates from *Kepler* and $K2$ of 2.48 ± 0.32 and 0.75 ± 0.11 planets per star respectively. Note that the former is consistent with previous measurements from *Kepler* (Morton & Swift 2014; Dressing & Charbonneau 2015; Gaidos et al. 2016). However, noting that the FP rate of small $K2$ PCs is small ($\sim 5.7\%$, Table 4), many $K2$ PCs should contribute to the calculation of the occurrence rates from $K2$ thus increasing its value and likely becoming less discrepant with the *Kepler*-derived value.

We consider the 126 PCs from the transiting planet search in $K2$ campaigns 0-8 (Kruse et al. 2019). Statistically correcting for FPs results in 119 PCs plus 52 confirmed planets around 7227 $K2$ stars within our stellar sample that were observed in any of the $K2$ campaigns 0-8. Given the period and radius of each of these 171 planets, we apply the completeness corrections computed in Sect. 4.2, divide out the number of low mass stars observed in campaigns 0-8, and measure a cumulative occurrence rate of 2.26 ± 0.38 planets per star.

The inclusion of PCs from Kruse et al. (2019) boosts the cumulative occurrence rate measurement from $K2$ to a value that is consistent with that from *Kepler* (i.e. 2.48 ± 0.32). This indicates that the *Kepler* and $K2$ planet populations are consistent and that the reduced detection sensitivity of $K2$ compared to *Kepler* is genuine (c.f. Figure 5). Note that the lesser $K2$ completeness continues to have a negative effect on the precision of the occurrence rate measurement despite $K2$ campaigns 0-8 having ~ 1.8 times as many low mass dwarf stars as *Kepler*. We also note that in this comparison we have not corrected for any stellar mass dependence of the occurrences rates which may produce a true discrepancy between the *Kepler* and $K2$ values as their respective stellar samples within this study are not equivalent (c.f. Figure 2). The agreement that we have demonstrated between the cumulative occurrence rates from *Kepler* and $K2$ has also been recently confirmed by Zink et al. (2020).

6. EVOLUTION OF THE RADIUS VALLEY AROUND LOW MASS STARS

6.1. Slope of the radius valley

Figure 11 shows the two-dimensional planetary occurrence rates in the $F - r_p$ space for our planet sample

⁸ Validated and confirmed planets are considered equivalent dispositions.

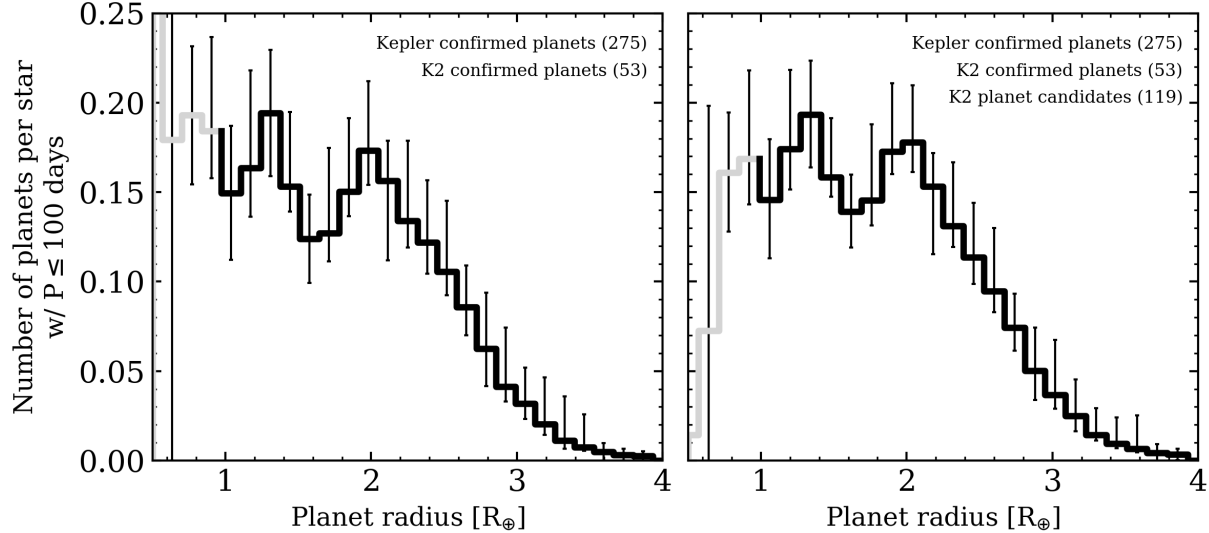


FIG. 10.— Comparison of the occurrence rates derived from planet samples with and without planet candidates included. *Left panel:* same as Figure 9. *Right panel:* histogram depicting the relative occurrence rate of close-in planets with orbital periods < 100 days derived from the population of confirmed planets from *Kepler* and *K2* and supplemented by 119 randomly selected PCs around low mass stars from Kruse et al. (2019). The radius valley continues to be resolved with the inclusion of PCs improving the median uncertainty on the occurrence rate bins although the bimodality becomes less prominent with numerous PCs partially filling the valley.

as well as for the close-in *Kepler* planets around Sun-like stars from Martinez et al. (2019). In this parameter space, we calculate the slope of the radius valley with F and compare the measured value to model predictions of the transition from rocky to non-rocky planets versus insolation. We measure the slope using a similar methodology to Martinez et al. (2019) wherein the two-dimensional occurrence rates are first resampled from its MAP value and uncertainties in 10^3 realizations. In each realization, the one-dimensional occurrence rate distribution $f_j(r_p)$ is computed in logarithmically spaced F bins. For each one-dimensional distribution, the f_j -weighted radii of the rocky and non-rocky peaks are then calculated. The central radius of the valley is computed as the average radius between the two peaks assuming a uniform weighting as we are interested in measuring the location of the valley and not the relative strength of the two peaks as a function of F . The resulting radius valley locations in the $\log F - \log r_p$ space are then fit with a linear model as depicted in Figure 11. Over the 10^3 realizations of resampled planet populations, we measure an average slope and standard deviation of $r_{p,\text{valley}} \propto F^{-0.060 \pm 0.025}$. Similarly, repeating this exercise in the $\log P - \log r_p$ space yields $r_{p,\text{valley}} \propto P^{0.058 \pm 0.022}$. For ease of reference, the slopes measured in this work and around FGK stars from the CKS (Martinez et al. 2019) are reported in Table 5.

The negative slope of $r_{p,\text{valley}} \propto F^{-0.06}$ indicates that the location of the radius valley drops to smaller planet radii with increasing insolation (i.e. towards smaller orbital separations). This behavior is broadly consistent with models of the formation small rocky planets in a gas-poor environment (Lee et al. 2014; Lee & Chiang 2016; Lopez & Rice 2018). This formation scenario leads to the transition from rocky to non-rocky planets emerging due to the superposition of rocky and non-rocky planet populations whose formation timescales differ. In this scenario, the transition radius as a function of orbital separation is set by the maximum mass of a bare rocky

TABLE 5
MEASUREMENTS AND MODEL PREDICTIONS OF THE RADIUS VALLEY SLOPE

| Description | $d \log r_p / d \log P$ | $d \log r_p / d \log F$ | Refs. |
|-------------------------------------|-------------------------|-------------------------|-------|
| <i>Empirical slope measurements</i> | | | |
| Slope around low mass stars | 0.058 ± 0.022 | -0.060 ± 0.025 | 1 |
| Slope around Sun-like stars | -0.11 ± 0.03 | 0.12 ± 0.02 | 2 |
| <i>Model-predicted slopes</i> | | | |
| Gas poor formation | 0.11 | -0.08 | 3 |
| Photoevaporation | -0.15 | 0.11 | 3 |
| Core-powered mass loss | -0.13 | 0.10 | 4 |
| Impact erosion | -0.33 | 0.25 | 5 |

NOTE. — r_p in units of R_\oplus , P in units of days, and F in units of F_\oplus .

References: 1) this work 2) Martinez et al. 2019 3) Lopez & Rice 2018 4) Gupta & Schlichting 2019b 5) Wyatt et al. 2019.

core which itself is set by the amount of available solid material for the proto-planet to form out of via collisional growth. According to the minimum-mass extra-solar nebula (Chiang & Laughlin 2013), the solid surface density radial profile is $\sigma_{\text{solid}} \propto a^{-1.6}$ where a is the orbital distance. The amount of solid material accreted by a proto-planet is proportional to its Hill radius $r_H = a(m_p/3M_s)^{1/3}$ such that integrating over the feeding zone within the disk surface results in the maximum mass of a bare rocky core $m_{p,\text{max}} \propto a^{0.6} M_s^{-0.5}$, or $r_{p,\text{valley}} \propto a^{0.16} M_s^{-0.14}$ after applying the rocky planet mass-radius relation ($m_p \propto r_p^{3.7}$; Zeng et al. 2016). Hence, the transition radius is predicted to occur at larger planet radii with increasing separation for a given host spectral type (Lopez & Rice 2018). The corresponding theoretical scaling of the transition radius with insolation for a given spectral type is $r_{p,\text{valley}} \propto F^{-0.08}$ which is consistent with our measured scaling of $r_{p,\text{valley}} \propto F^{-0.060 \pm 0.025}$.

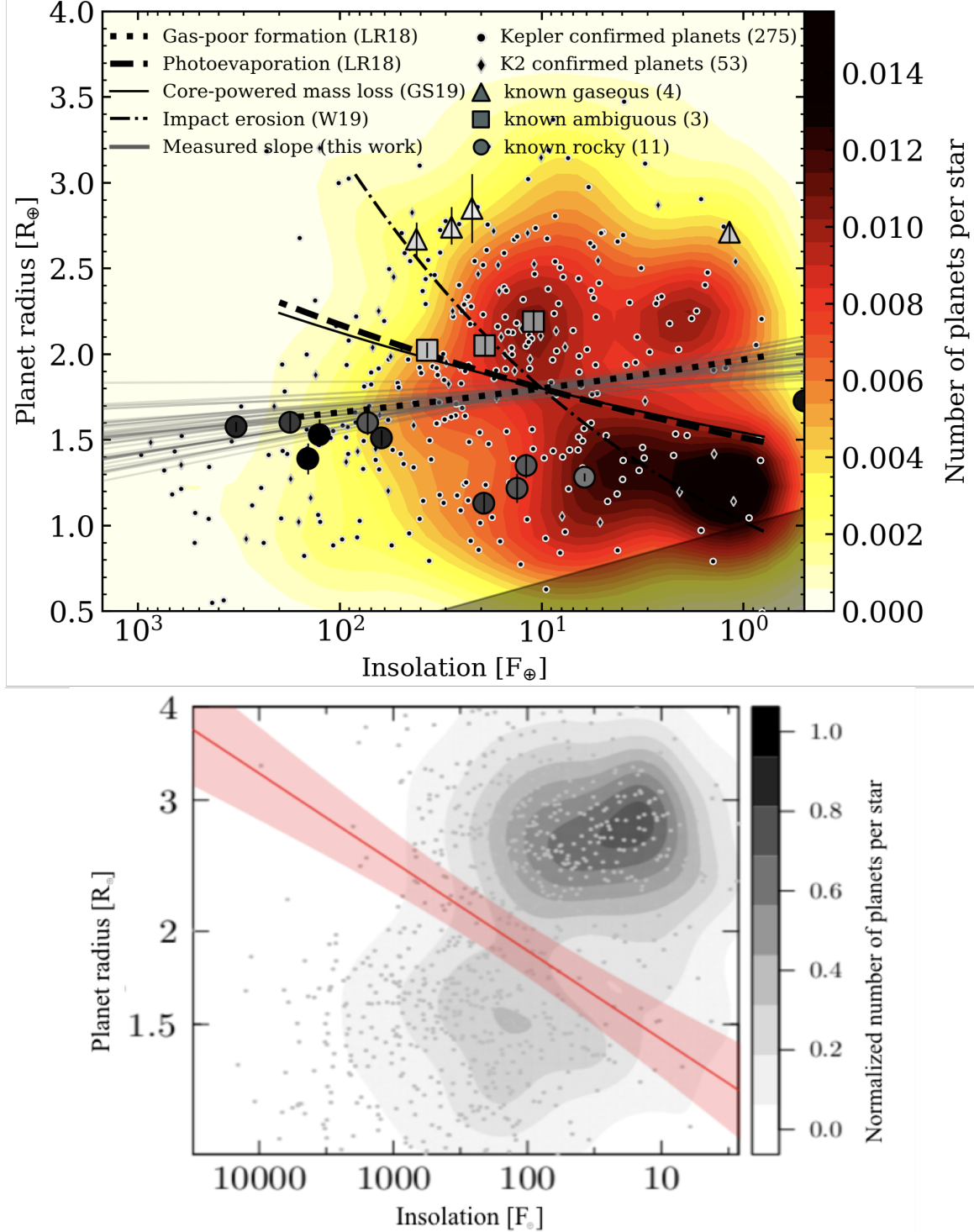


FIG. 11.— (Interactive figure) Planet occurrence rates versus insolation and planet radius around low mass and Sun-like stars. *Upper panel:* the maximum a-posteriori occurrence rate map calculated from the population of confirmed planets from *Kepler* and *K2* around low mass dwarf stars [small circles and diamonds]. Overplotted in black are model predictions of the transition from rocky to non-rocky planets in the following scenarios: core-powered mass loss (Gupta & Schlichting 2019b), photoevaporation (Lopez & Rice 2018), and gas-poor formation Lopez & Rice (2018). We measure the slope of the radius valley to be $r_{p,\text{valley}} \propto F^{-0.060 \pm 0.025}$ which is consistent with predictions from gas-poor formation of terrestrial planets. Also overplotted are planets with $\geq 3\sigma$ bulk density measurements from the literature that are classified as having either a rocky (circles), a gaseous (triangles), or an intermediate (squares) bulk composition. Marker colors are indicative of the MAP planet bulk densities. *Lower panel:* the occurrence rate map of close-in *Kepler* planets around Sun-like stars ($r_{p,\text{valley}} \propto F^{0.12 \pm 0.02}$; Martinez et al. 2019). Note the unique F and r_p scales depicted in each panel.

In addition to being consistent with predictions from gas-poor terrestrial planet formation models, the measured slope is inconsistent with models of thermally driven atmospheric escape from photoevaporation or core-powered mass loss. These models predict an increasing transition radius with increasing insolation ($r_{p,\text{valley}} \propto F^{0.11}$; Lopez & Rice 2018, $r_{p,\text{valley}} \propto F^{0.10}$; Gupta & Schlichting 2019b respectively). The negative slope of the radius valley around low mass stars differs in sign from the trend seen around Sun-like stars ($r_{p,\text{valley}} \propto F^{0.12 \pm 0.02}$, $r_{p,\text{valley}} \propto P^{-0.11 \pm 0.03}$; Martinez et al. 2019). These differing observational findings in each stellar mass regime may either be interpreted as a signature of distinct planet formation processes, wherein gas-poor planet formation is more prominent around low mass stars, or that the efficiency of atmospheric post-processing is weakened around lower mass stars.

The inclusion of planets with $\geq 3\sigma$ bulk density measurements (see Table 3) in Figure 11 reveals that all planets that are inconsistent with having bulk rocky compositions lie above the transition radius predictions from all physical models considered (i.e. gas-poor formation, photoevaporation, core-powered mass loss, and impact erosion). However, the temperate rocky planet LHS 1140b ($F = 0.5 F_\oplus$, $r_p = 1.73 R_\oplus$) sits in the $F - r_p$ parameter space below the predicted transition radius from gas-poor formation but above the predicted transition from photoevaporation, core-powered mass loss, and impact erosion. Although LHS 1140b is the only instance of a planet existing between the radius valley predictions from gas-poor formation and thermally driven or impact driven mass loss in Figure 11, the location and rocky composition of LHS 1140b provide supporting evidence for the applicability of models of gas-poor terrestrial planet formation to the emergence of the radius valley around low mass stars.

6.2. Planet populations versus stellar mass

In addition to calculating the occurrence rates f_{ij} among our full stellar sample, here we consider the evolution of the planet population in unique host stellar mass bins. Figure 12 shows the MAP f_{ij} maps in $P - r_p$ space and the marginalized f_j distributions in four stellar mass bins representing our full stellar sample ($M_s \in [0.08, 0.93] M_\odot$), the massive half of the sample ($M_s > 0.65 M_\odot$), the low mass half of the sample ($M_s < 0.65 M_\odot$), and a subset of the latter focusing on increasingly lower mass stars ($M_s < 0.42 M_\odot$). The statistically significant resolution of the radius valley in the f_j occurrence rates is only accomplished in the full stellar sample. The reduction of the sample size in the three remaining M_s bins inflates the f_j uncertainties such that the valley is observed at $< 1\sigma$ and hence not significant. However, the characteristic bimodality continues to be exhibited in the MAP f_{ij} for the more massive half of our stellar sample. Furthermore, the f_{ij} structures from the full and massive samples are similar as the majority of our full planet sample orbit stars more massive than the median stellar mass of $0.65 M_\odot$ (i.e. $\sim 62\%$ of our confirmed planet sample).

In considering stars less massive than $0.65 M_\odot$, the non-rocky planet peak begins to diminish relative to the terrestrial-sized planets. As evidenced in the MAP f_j distribution around stars with $M_s \in [0.08, 0.65] M_\odot$,

TABLE 6
RELATIVE OCCURRENCE RATES OF CLOSE-IN ROCKY AND NON-ROCKY PLANETS AROUND LOW MASS STARS

| Stellar mass range [M_\odot] | f_{rocky} $r_p \in [1, 1.6]$ | $f_{\text{non-rocky}}$ $r_p \in [1.6, 2.5]$ | $f_{\text{rocky}}/f_{\text{non-rocky}}$ |
|----------------------------------|--|--|---|
| [0.08, 0.90] | 0.68 ± 0.07 | 1.02 ± 0.08 | 0.66 ± 0.09 |
| [0.63, 0.90] | 0.69 ± 0.11 | 1.28 ± 0.16 | 0.54 ± 0.11 |
| [0.08, 0.63] | 1.10 ± 0.16 | 1.02 ± 0.16 | 1.08 ± 0.23 |
| [0.08, 0.42] | 1.64 ± 0.43 | 0.19 ± 0.09 | 8.46 ± 4.62 |

the radius valley might persist around $1.6 R_\oplus$ but the non-rocky planet peak does not appear distinct from the rocky planet peak in the MAP f_{ij} map. In other words, the relative frequency of rocky to non-rocky planets appears to increase significantly around M dwarfs compared to the more massive K dwarfs. This feature is further accentuated around the lowest mass stars in our sample ($< 0.42 M_\odot$) for which terrestrial-sized planets clearly dominate the distribution of close-in planets. The relative frequency of rocky to non-rocky planets in each stellar mass bin are reported in Table 6 for fixed definitions of $r_p \in [1, 1.6] R_\oplus$ and $r_p \in [1.6, 2.5] R_\oplus$ respectively. The inner limit of $1 R_\oplus$ restricts this analysis to where the detection sensitivity is still informative. The outer limit of $2.5 R_\oplus$ is chosen such that the full width at half maximum of the non-rocky planet peak in the f_j distribution from the full stellar sample is approximately identical for each peak (Figure 9). **This selection is purely empirical and disregards any physical motivation for a maximum radius of the non-rocky planet peak from, say, the dissolution of H/He into the planet's magma ocean at the high surface pressures expected for planets with $r_p \gtrsim 3 R_\oplus$ (Kite et al. 2019).**

The values in Table 6 indicate the significant increase in the relative occurrence of rocky planets with decreasing stellar mass that is illustrated in Figure 12. Our measurements show that non-rocky planets are nearly twice as common as rocky planets around mid to late K dwarfs ($M_s \in [0.65, 0.93] M_\odot$) while the relative frequency approaches unity around the full suite of M dwarfs ($M_s \in [0.08, 0.65] M_\odot$). Focusing on mid-to-late M dwarfs only in the lowest stellar mass bin considered, rocky planets become much more prominent as they outnumber non-rocky planets by a factor of $\sim 8.5 \pm 4.6$. This result is broadly consistent with the calculations from Hardegree-Ullman et al. (2019) who find that terrestrial-sized planets ($r_p \in [0.5, 1.5] R_\oplus$) are about 4 – 5 times as common as non-rocky planets ($r_p \in [1.5, 2.5] R_\oplus$) around M3-5.5 dwarfs ($M_s \in [0.12, 0.38] M_\odot$). Our calculations provide supporting evidence for an increase in the frequency of close-in rocky planets around increasingly lower mass stars even with the small number of confirmed transiting planets in that mass regime. More robust statements regarding the absolute occurrence rate of rocky planets around mid-to-late M dwarfs will require a larger stellar sample in transit surveys with sensitivity to wider separations out to hundreds of days where giant planets begin to emerge around these stars (Bonfils et al. 2013; Morales et al. 2019).

Although our data show a significant increase in the relative occurrence of rocky to non-rocky planets around increasingly lower mass stars, we are unable to firmly

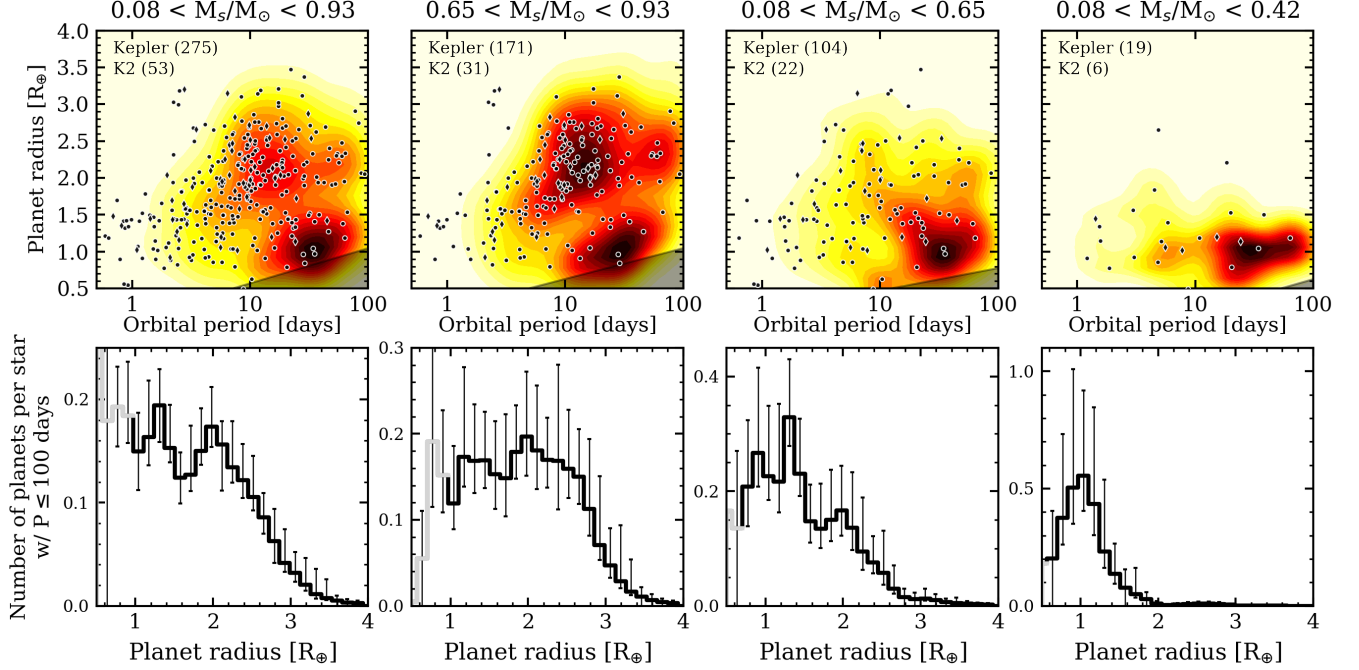


FIG. 12.— (Interactive figure) 2D and 1D planet occurrence rates in various stellar mass bins. *Top panels:* planet occurrence rate maps as a function of orbital period and planet radius. Overplotted are the relevant subsets of the population of confirmed planets from *Kepler* and *K2* [small circles and diamonds]. *Bottom panels:* distributions of the relative planet occurrence rate as a function of planet radius. Note the differing occurrence rate scales. Each column corresponds to a unique cut in stellar masses which represent the full stellar sample ($M_s \in [0.08, 0.93] M_\odot$), the massive half of the stellar sample ($M_s \in [0.65, 0.93] M_\odot$), the low mass half of the stellar sample ($M_s \in [0.08, 0.65] M_\odot$), and the lowest mass bin ($M_s \in [0.08, 0.42] M_\odot$) depicting a subset of the low mass half of the stellar sample. Rocky planets appear to increase in prominence around lower mass stars.

identify the cause of this trend with these data. In other words, there are two outstanding hypotheses that cannot be ruled out by our data. The first scenario requires the preferential formation of rocky planets around low mass stars such that atmospheric processing by photoevaporation, core-powered mass loss, or impact erosion, have little to no effect. The alternative scenario is that planet formation processes around low mass stars continues to produce non-rocky planets with significant primordial atmospheres that are subsequently stripped by any of the aforementioned processes. The slope of the valley measured from Figure 11 suggests that the former scenario is important but our calculations of the occurrence rates in various stellar mass bins are unable to solely confirm or reject any physical mechanism at this time.

6.3. Dependence of radius valley features on stellar mass

Here we measure the locations and uncertainties of features in the radius valley in each of the stellar mass bins considered in Sect. 6.2. For each stellar mass bin we measure the occurrence rate-weighted radius of the rocky planet peak, the non-rocky planet peak (where applicable), and the radius valley. The uncertainties in the feature locations are largely determined by uncertainties in the measured occurrence rates but are also directly affected by the following hyperparameters: the f_{ij} smoothing parameter, the minimum detection sensitivity still considered reliable, the P bin width, the r_p bin width, and the imposed upper and lower P and r_p limits on each peak. The upper and lower r_p limits are defined based on the visual inspection of the f_{ij} maps in Figure 12 and are used to demarcate the boundaries of each peak—and

by extension—the valley separating the peaks. As an example, if the prescribed boundaries on the rocky peak are set to 1–50 days and $0.8\text{--}1.4 R_\oplus$, then only the occurrence rates over that subset of the $P - r_p$ parameter space are used to calculate the f_{ij} -weighted rocky peak radius. The range of boundary values for each peak are listed in Table 7. In practice, we derive 10^3 realizations of each f_{ij} map with each realization having a unique set of the aforementioned hyperparameters. The resulting f_{ij} maps are marginalized over P and the f_j -weighted radius of each peak is computed over the domain bounded by the relevant hyperparameters. The same is done for the radius valley using the inverse occurrence rates.

The resulting locations of each radius peak and the valley are depicted in Figure 13 as a function of stellar mass. The feature locations and uncertainties are also given explicitly in Table 8. The depicted M_s values are represented by the median stellar mass within each bin with uncertainties derived from the 16th and 84th percentiles. In computing the feature locations we assume that the bimodal r_p distribution is present in all stellar mass bins aside from the lowest mass bin wherein the non-rocky peak becomes insignificant (see Figure 12). In the lowest stellar mass bin, we only measure the location of the rocky planet peak and its edge which marks the transition from rocky to non-rocky planets despite the latter being inherently rare around these types of stars. These feature radii are then compared to those measured by Fulton & Petigura (2018) around Sun-like stars with $M_s < 0.97 M_\odot$, $M_s \in [0.97, 1.11] M_\odot$, and $M_s > 1.11 M_\odot$.

Figure 13 reveals that the location of each feature, measured from our full stellar sample, continues the

TABLE 7
ASSUMED BOUNDARY RANGES ON THE LOCATIONS OF RADIUS VALLEY FEATURES

| Stellar mass range [M _⊙] | log P lower boundary [days] | log P upper boundary [days] | Rocky peak lower r_p boundary [R _⊕] | Rocky peak upper r_p boundary [R _⊕] | Non-rocky peak lower r_p boundary [R _⊕] | Non-rocky peak upper r_p boundary [R _⊕] |
|--------------------------------------|---------------------------------|----------------------------------|---|---|---|---|
| [0.08, 0.90] | $\mathcal{U}(\log 0.5, \log 2)$ | $\mathcal{U}(\log 50, \log 100)$ | $\mathcal{U}(0.8, 1)$ | $\mathcal{U}(1.2, 1.5)$ | $\mathcal{U}(1.6, 1.9)$ | $\mathcal{U}(2.3, 2.5)$ |
| [0.63, 0.90] | $\mathcal{U}(\log 0.5, \log 2)$ | $\mathcal{U}(\log 50, \log 100)$ | $\mathcal{U}(0.8, 1)$ | $\mathcal{U}(1.3, 1.5)$ | $\mathcal{U}(1.8, 2)$ | $\mathcal{U}(2.4, 2.7)$ |
| [0.08, 0.63] | $\mathcal{U}(\log 0.5, \log 2)$ | $\mathcal{U}(\log 50, \log 100)$ | $\mathcal{U}(0.6, 0.9)$ | $\mathcal{U}(1.2, 1.4)$ | $\mathcal{U}(1.8, 2)$ | $\mathcal{U}(2.1, 2.3)$ |
| [0.08, 0.42] | $\mathcal{U}(\log 0.5, \log 2)$ | $\mathcal{U}(\log 50, \log 100)$ | $\mathcal{U}(0.5, 0.7)$ | $\mathcal{U}(1.3, 1.4)$ | $\mathcal{U}(1.7, 1.8)$ | $\mathcal{U}(1.8, 2)$ |

NOTE. — The r_p boundaries on the radius valley are given implicitly by the upper r_p limit on the rocky peak and the lower r_p limit on the non-rocky peak.

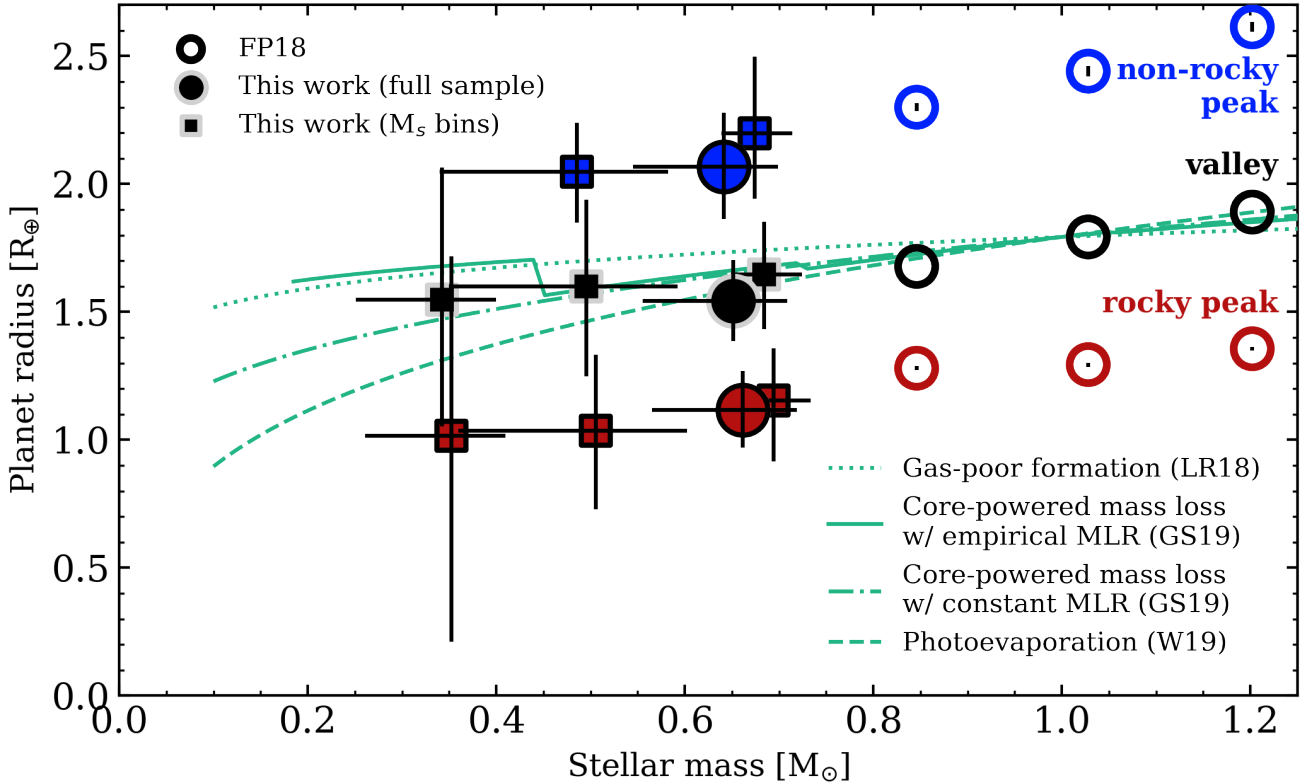


FIG. 13.— (Interactive figure) Evolution of the radius valley features with stellar mass. Solid markers: the occurrence rate-weighted locations of the non-rocky planet peak (blue markers), the radius valley (black markers) and the rocky planet peak (red markers) as a function of host stellar mass. Measurements around Sun-like stars with $M_s > 0.8$ M_⊕ are retrieved from Fulton & Petigura (2018) [open circles]. Feature radii from our full sample with a median value of $M_s = 0.651^{+0.058}_{-0.096}$ M_⊕ are depicted as filled circles. Filled squares depict the feature radii from partitioning our stellar sample into three M_s bins: $M_s \in [0.65, 0.93]$ M_⊕, $M_s \in [0.08, 0.65]$ M_⊕, and $M_s \in [0.08, 0.42]$ M_⊕. Markers in each stellar mass bin are slightly offset along the M_s axis to assist in visualizing the errorbars. Uncertainties on the peak and valley locations are derived by sampling the measured occurrence rates and their uncertainties along with samples of the hyperparameters controlling map smoothing, minimum detection sensitivity, planet parameter binning, and the assumed feature ranges in P and r_p . The green curves represent theoretical predictions for the evolution of the radius valley with stellar mass based on physical models of gas-poor terrestrial planet formation (dotted; Lopez & Rice 2018), core-powered atmospheric mass loss with an empirical mass-luminosity relation (solid; Gupta & Schlichting 2019b), a constant mass-luminosity relation (dash-dotted; Gupta & Schlichting 2019b), and photoevaporation (dashed; Wu 2019). The models only predict scaling relations with M_s and as such are anchored to the measured valley location at $M_s \sim M_\odot$.

trend of monotonically decreasing towards smaller r_p with decreasing M_s . The slopes of this decrease for the rocky and non-rocky planet peaks, measured with the three points from Fulton & Petigura (2018) and from our full stellar sample, are $dr_{p,rock}/dM_s = 0.40$ and $dr_{p,gas}/dM_s = 0.97$ respectively. The relative slopes indicate that the most common size of non-rocky planet decreases more steeply with M_s than the typical size of rocky planets. This trend is indicative of the effective

disappearance of non-rocky planets around increasingly lower mass stars (see Figure 12) while terrestrial-sized planets appear to persist. Furthermore, the reduced slope of the rocky peak may be evidence for a characteristic planetary core size of ≈ 1 R_⊕ although its exact location is largely uncertain due to the limited detection sensitivity to sub-Earth-sized planets. Furthermore, the probabilistic classification of rocky planets as being primordially rocky or an evaporated core requires addi-

TABLE 8
RADIUS VALLEY FEATURES VERSUS STELLAR MASS

| Stellar mass [M _⊙] | Rocky peak [R _⊕] | Radius valley [R _⊕] | Non-rocky peak [R _⊕] |
|--|--|--|--|
| 0.651 ^{+0.058} ^{-0.096} | 1.118 ^{+0.151} ^{-0.148} | 1.543 ^{+0.160} ^{-0.169} | 2.068 ^{+0.211} ^{-0.205} |
| 0.684 ^{+0.040} ^{-0.035} | 1.154 ^{+0.205} ^{-0.239} | 1.647 ^{+0.207} ^{-0.215} | 2.197 ^{+0.301} ^{-0.256} |
| 0.500 ^{+0.097} ^{-0.146} | 1.036 ^{+0.297} ^{-0.308} | 1.599 ^{+0.340} ^{-0.352} | 2.048 ^{+0.191} ^{-0.199} |
| 0.343 ^{+0.057} ^{-0.092} | 1.017 ^{+0.700} ^{-0.807} | 1.548 ^{+0.515} ^{-0.496} | - |

NOTE. — As depicted in Fig. 13.

tional information about the planet’s orbit and stellar host properties (Neil & Rogers 2019). For example, there may be exist a stellar dependence on typical core sizes. This is because for Earth-like cores, the core size is intimately related to the core mass and final core masses depend on the availability of heavy elements which is known to be higher around M dwarfs than around FGK stars (Mullers et al. 2015a,b; Neil & Rogers 2018).

Models of the formation of the radius valley based on photoevaporation (Wu 2019), gas-poor formation (Lopez & Rice 2018), and core-powered mass loss (Gupta & Schlichting 2019b), all make explicit predictions for the evolution of the radius valley location with stellar mass. Predictions from the core-powered mass loss scenario are dependent on the stellar mass-luminosity relation (MLR) $L_s \propto M_s^\alpha$. In Figure 13, we consider predictions assuming either a constant MLR with $\alpha = 5$ (Gupta & Schlichting 2019b) or the empirically-derived piecewise MLR from Eker et al. (2018). All models predict a decreasing radius valley with decreasing stellar mass, but the models differ in the predicted rates of this decrease. At the median stellar mass of our full stellar sample (0.65 M_⊙), the measured location of the radius valley is 1.54 ± 0.16 R_⊕. This value—combined with measurements from Sun-like stars—favors a steep $dr_{p,\text{valley}}/dM_s$ slope although we are unable to distinguish between competing physical models given the measurement uncertainties. Fortunately, the model predictions continue to diverge with decreasing stellar mass such that measurements of the valley’s location in decreasing M_s bins may be used to rule out the operation of certain physical mechanisms in the low stellar mass regime. Although the trend of decreasing feature radii with decreasing stellar mass appears to be upheld, the poor counting statistics in the reduced M_s bins prevent significant inferences with regards to the relative strength of the competing physical processes. This problem can only be addressed by increasing the number of mid-to-late M dwarfs in transit surveys and by maximizing the detection sensitivity to planets spanning the radius valley (see Sect. 7.1).

7. DISCUSSION

7.1. Improving constraints on the sculpting of the radius valley using mid-M dwarfs

The issue of having insufficient information to distinguish between photoevaporation, core-powered mass loss, and gas-poor formation around low mass stars can be addressed with two steps. Firstly, by expanding the low mass stellar sample in transiting planet searches and secondly, by quantifying the detection sensitivity in those

searches. NASA’s Transiting Exoplanet Survey Satellite (*TESS*; Ricker et al. 2015) is expected to provide hundreds of new transiting planet discoveries in the vicinity of the radius valley (Barclay et al. 2018). *TESS* is particularly well-suited to the discovery of close-in planets around low mass stars down to M5V ($M_s \sim 0.16$ M_⊙) due to its red bandpass (600-1000 nm) and its high cadence (2-minute) observations of 200,000-400,000 stars over $\sim 94\%$ of the sky by the completion of its recently approved extended mission.

The *TESS* primary mission—lasting one year—has been ongoing since July 2018. Based on the photometric performance of the mission and consequently on the success of planet searches by the Science Processing Operations Center (SPOC; Jenkins et al. 2016; Twicken et al. 2018; Li et al. 2018) at the time of writing, we can estimate the number of low mass stars required to be observed by *TESS* to enable robust conclusions regarding the nature of the emergence of the radius valley. These calculations proceed by noting that the measurement uncertainty on the feature locations from binomial statistics scales as $\sqrt{N_s P(1 - P)}$ where N_s is the number of observed stars and P is the probability of detecting a planet close to the radius valley given the detection sensitivity, the transit probability, and their inherent rate of occurrence (see Eq. 7). Through sectors 1-14, *TESS* has observed $N_{s,\text{TESS}} = 23,051$ stars less massive than 0.4 M_⊙ with 2-minute cadence from its Candidate Target List (CTL; Stassun et al. 2019). Among these stars, the SPOC has reported three objects of interest close to the radius valley between $1.4 - 1.6$ R_⊕⁹. Assuming a 0% false positive rate among these planet candidates, and the same MAP occurrence rate measured with *Kepler* ($f_{\text{valley}} \approx 0.19$ planets per star), we find the probability of *TESS* to detect a transiting planet spanning the radius valley around a star with $M_s < 0.4$ M_⊙ to be $P_{\text{valley,TESS}} = 1.30 \times 10^{-4}$. We can compare these numbers to the *Kepler* values of $N_{s,\text{Kep}} = 33$ and $P_{\text{valley,Kep}} = 8.56 \times 10^{-3}$ to scale the uncertainty on f_{valley} —and hence on the radius valley location—as an increasing number of mid-to-late M dwarfs are observed with 2-minute cadence with *TESS*.

The resulting improvement in the measurement precision of the radius valley with observations of additional mid-to-late M dwarfs is shown in Figure 14. The *TESS* curve reveals how precisely the location of the radius valley can be measured given *TESS*’s approximate detection sensitivity to planets spanning the radius valley and as the number of low mass stars observed with 2-minute cadence is increased. Note that the improvement allotted by *TESS* should only be interpreted as an approximation given that its detection sensitivity has not yet been adequately characterized. In our calculations, the *TESS* detection sensitivity is estimated as a constant value as described in the preceding paragraph.

We define a target measurement precision as that which is required to distinguish between predictions from photoevaporation and core-powered mass loss (assuming an empirical mass-luminosity relation) at 3σ around low mass stars with a median stellar mass of 0.35 M_⊙. Based on the model curves in Figure 13, this required precision

⁹ TOIs: 175.01, 406.01, and 667.01.

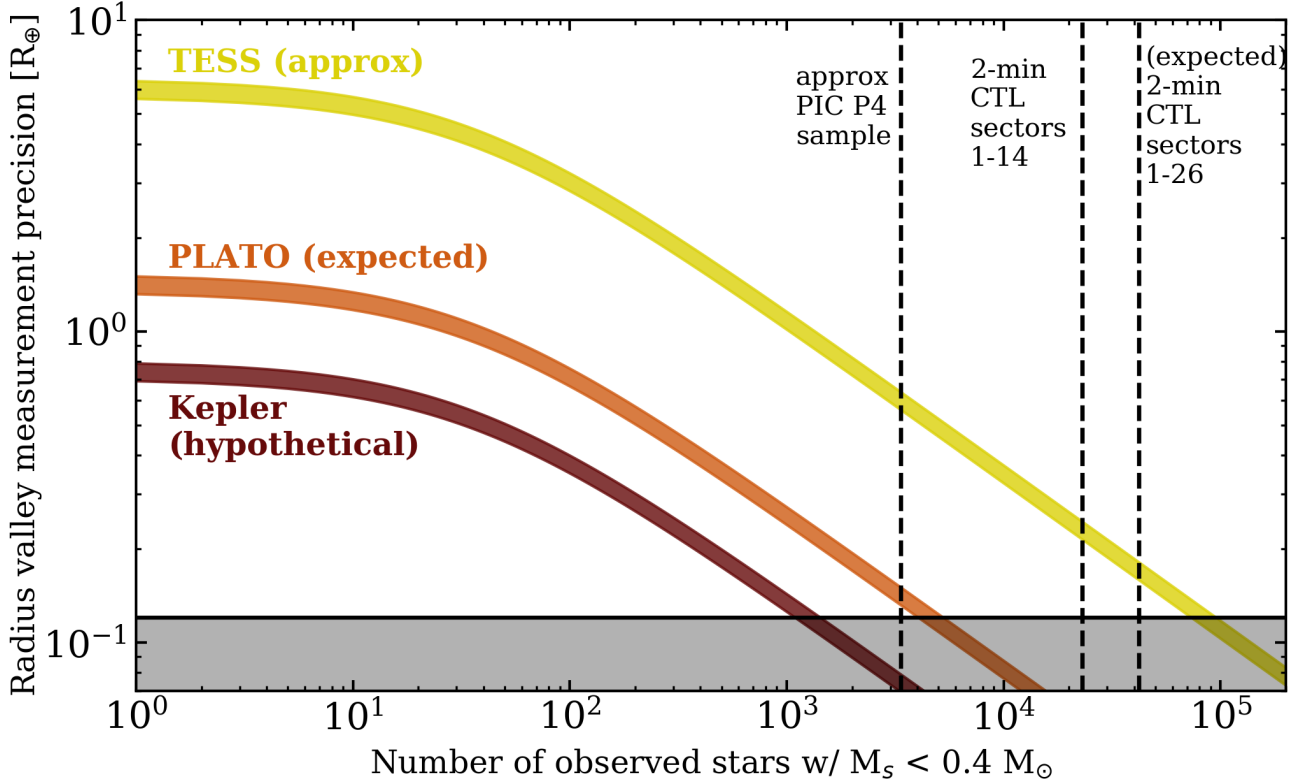


FIG. 14.— Expected improvement in the measurement precision of the radius valley location with the number of observed low mass stars. Measurement precision curves of the upper and lower uncertainties on the location of the radius valley are derived from binomial statistics. These calculations use approximate and expected detection sensitivity values for the *TESS* (yellow) and *PLATO* (orange) missions. The curve representing a hypothetical continuation of the primary *Kepler* mission is depicted in red. The target precision of $0.12 R_{\oplus}$ (shaded region) would enable models of photoevaporation to be distinguished from core-powered mass loss or gas-poor formation at 3σ at $M_s = 0.35 M_{\odot}$. Measurement precision curves are compared to the sample sizes of mid-to-late M dwarfs from the *TESS* Candidate Target List for sectors 1-14 (i.e. to the time of writing) and 1-26 (i.e. to the end of the *TESS* primary mission). Also included is the approximate number of mid-to-late M dwarfs included in the P4 sample of the *PLATO* Input Catalog.

corresponds to a radius valley uncertainty of $\sim 0.12 R_{\oplus}$. A very similar level of precision would be required to distinguish between photoevaporation and gas-poor formation as well. The approximate *TESS* detection sensitivity implies that *TESS* will be required to observe $\sim 85,000$ mid-to-late M dwarfs to distinguish between model predictions of photoevaporation and core-powered mass loss or gas-poor formation at 3σ . At the time of writing, only 23,051 such stars have been targeted with 2-minute cadence. Extrapolating to the end of *TESS*'s primary mission, we expect a total of $\sim 42,000$ such stars to be observed with 2-minute cadence. If the *TESS* detection sensitivity is well-characterized by that time and is roughly consistent with the approximate value assumed here, then *TESS* could achieve a radius valley uncertainty of $\sim 0.17 R_{\oplus}$ by the end of its prime mission. This would still be useful for constraining radius valley formation models as predictions from photoevaporation and core-powered mass loss—or gas-poor formation—could be distinguished at $\sim 2.1\sigma$ with this level of precision. Note that these calculations do not include non-CTL stars that may be targeted in the 30 minute *TESS* Full Frame Images and could also contribute to the occurrence rate measurements, albeit with a reduced detection sensitivity.

Also included in Figure 14 is the curve for a hypothetical continuation of the primary *Kepler* mission. The calculation reveals that had *Kepler* been able to continue its

prime mission and had access to thousands of additional mid-M dwarfs than were targeted in the primary *Kepler* field, then the location of the radius valley could have been precisely measured with ~ 1200 observed stars.

The stellar input catalog for the up-coming ESA *PLATO* mission (Rauer et al. 2014) has yet to be defined. The primary goal of *PLATO* is to detect and characterize transiting habitable zone planets around bright FGK stars. Despite this, according to the mission's Definition Study Report¹⁰, a subset of the *PLATO* Input Catalog (PIC) known as sample P4 will target ≥ 5000 M dwarfs brighter than $V = 16$ as part of the mission's Long-Duration Observing Phase (LOP) lasting a minimum of two years. Furthermore, the expected random noise in P4 is 800 ppm on one hour timescales. To compute the probability of detecting a radius valley planet around a mid-to-late M dwarf targeted by *PLATO*, we first assume that for a given transit S/N, *PLATO*'s detection sensitivity will be equivalent to that of *Kepler* (Figure 5). We fix the transit S/N (Eq. 4) of a radius valley planet orbiting a mid-M dwarf using the values $r_p = 1.5 R_{\oplus}$, $R_s = 0.35 R_{\odot}$, $M_s = 0.35 M_{\odot}$, $CDPP_{1 \text{ hr}} = 800$ ppm, and $n_{\text{transits}} = 73$ for stars in the LOP observing phase. We note the inexact nature of this calculation which neglects the observing cadence and variations in

the transit depth and photometric precision with each P4 star. Nevertheless, assuming the *Kepler* occurrence rate we estimate that $P_{\text{valley,PLATO}} = 2.35 \times 10^{-3}$. This probability is ~ 18 times the estimated value for *TESS* but is about one quarter that of *Kepler*. The expected radius valley measurement precision with *PLATO* is also depicted in Figure 14.

Although the exact P4 M dwarf sample is not yet defined, recent developments at the September 2019 PIC Workshop in Italy¹¹ concluded that the properties of the sample will be consistent with M dwarf stars in the solar vicinity. Although this statement is very rough and not binding to the final definition of the PIC, we combine this expectation with knowledge of M dwarfs in the solar neighborhood to estimate the number of mid-to-late M dwarfs in the P4 sample. We do so by retrieving the M dwarf sample within 25 pc from Winters et al. (2019). Noting that this volume-limited sample is $\sim 33\%$ complete (J. Winters private communication), we identify ~ 2829 M dwarfs within 25 pc and with $V < 16$. We then scale up the M dwarf population beyond 25 pc until 5000 stars with $V < 16$ are included assuming a homogeneous M dwarf population beyond 25 pc. Of those stars representing probable targets within the P4 sample, 3358 have masses $< 0.4 M_\odot$. With this many mid-to-late M dwarfs targeted by *PLATO* we expect the radius valley uncertainty to reach $\sim 0.14 R_\oplus$ which would enable models of photoevaporation to be distinguished from models of core-powered mass low or gas-poor formation at $\sim 2.6\sigma$.

7.2. Implications for RV planet searches around low mass stars

Many existing and up-coming radial velocity (RV) spectrographs will be partially focused on characterizing the masses of planets spanning the radius valley in order to improve our physical understanding of the nature of those planets. In particular, a subset of those spectrographs operating in the near-IR will focus heavily on M dwarf planetary systems (e.g. CARMENES; Quirrenbach et al. 2014, HPF; Mahadevan et al. 2012, IRD; Kotani et al. 2014, MAROON-X; Seifahrt et al. 2018, NIRPS; Bouchy et al. 2017, SPIRou; Donati et al. 2018). In defining target samples that are equally complete on either side of the radius valley, it is critically important that the location of the transition between rocky and non-rocky planets is known. In our full stellar sample, which includes mid-to-late K dwarfs, the radius valley is centered at $1.54 \pm 0.16 R_\oplus$. Although we remind the reader that the exact value is dependent on the planet’s separation (see Figure 11). A consistent value of $1.55^{+0.52}_{-0.50}$ is also recovered—albeit with reduced significance—around stars later than about M2.5V. This value is slightly lower than the valley locations measured around Sun-like stars of $\sim 1.9 R_\oplus$ for $M_s \sim 1.2 M_\odot$ and $\sim 1.7 R_\oplus$ for $M_s \sim 0.85 M_\odot$ (Fulton & Petigura 2018).

Furthermore, the opposing slope signs of the radius valley around Sun-like and low mass stars (c.f. Figure 11 and Table 5) has implications for where in the planetary parameter space one expects to find predominantly rocky and non-rocky planets. Figure 15 highlights the region of interest for resolving the rocky to non-rocky transition

in the $P - r_p$ space. This region is defined by the intermediate region between the radius valley slope measured in this work to the slope measured around Sun-like stars from the CKS sample (Martinez et al. 2019) where the latter is first scaled from its median stellar mass of $1.01 M_\odot$ to the median stellar mass of our sample ($0.65 M_\odot$) using the M_s -dependent scaling relation of the radius valley under photoevaporation (Wu 2019).

The measured transitions from each stellar mass regime intersect at $P \sim 23.52$ days such that two regions of interest emerge and are bounded by

$$r_p \in \begin{cases} [r_{p,\text{valley},\text{this work}}, r_{p,\text{valley},\text{M19}}], & P < 23.52 \text{ days}, \\ [r_{p,\text{valley},\text{M19}}, r_{p,\text{valley},\text{this work}}], & P > 23.52 \text{ days}. \end{cases} \quad (9)$$

where

$$r_{p,\text{valley},\text{this work}} = 0.11 \cdot \log_{10}(P) + 1.52, \quad (10)$$

$$r_{p,\text{valley},\text{M19}} = -0.48 \cdot \log_{10}(P) + 2.32. \quad (11)$$

These subsets of the $P - r_p$ space define the regions of interest for resolving the rocky to non-rocky transition around low mass stars. For example, at $P \lesssim 23.52$ days thermally driven atmospheric mass loss, such as that from photoevaporation, predicts that planets in the set defined by Eq. 9 should be predominantly rocky. Whereas the gas-poor formation scenario, whose predicted radius valley slope differs in sign from that of thermally driven mass loss, predicts that those planets should be predominantly non-rocky. These predictions can be robustly tested by targeting planets within the Eq. 9 regions of interest and obtaining precise planetary bulk density measurements. As seen in Figure 15, there are only ~ 5 planets in the region of interest with $\geq 3\sigma$ bulk density measurements. These planets reveal the decrease in bulk density with increasing r_p although insufficient information is available to resolve a possibly sharp transition. At the time of writing, *TESS* has identified such eleven TOIs¹² around stars with $T_{\text{eff}} < 4700$ K that satisfy Eq. 9. Ten of these TOIs have $J < 11$ and should be strongly considered as targets for RV follow-up campaigns¹³. Note that all ten TOIs have $P < 23.52$ days.

7.3. Imperfect clearing of the radius valley

As noted in Sect. 5.1 and evidenced in Figure 8, the radius valley is not completely void of confirmed planets. If the radius valley around low mass stars is produced solely from the late formation of terrestrial planets in a gas-poor environment—as the measured slope of the radius valley suggests (Figure 11)—then the partial filling of the valley may point to a continuum of formed planet sizes rather than two distinct populations of rocky and non-rocky planets. However if the radius valley is instead sculpted by atmospheric post processing—as the radius valley around Sun-like stars seems to be (Fulton et al. 2017; Fulton & Petigura 2018; Van Eylen et al. 2018; Martinez et al. 2019)—then the partial filling of the valley would imply that post processing from photoevapo-

¹² *TESS* Object-of-Interest.

¹³ TOIs: 134.01 (Astudillo-Defru et al. 2020), 237.01, 544.01, 702.01, 807.01, 833.01, 836.02, 873.01, 1075.01, and 1201.01.

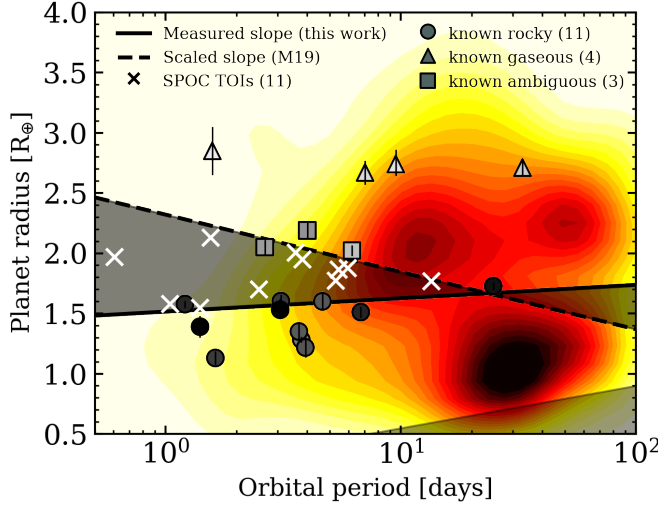


FIG. 15.— (*Interactive figure*) Regions of interest for resolving the transition between rocky and non-rocky planets around low mass stars. The colormap depicts the occurrence rate of small close-in planets from Figure 8. The rocky to non-rocky transition measured in this work is highlighted by the *solid black line*. The transition measured around FGK stars from Martinez et al. (2019) is highlighted by the *dashed black line* after being scaled to the median stellar mass of our sample. The shaded regions bounded by these curves represent the subset of the $P - r_p$ parameter space of interest for resolving the transition around low mass stars with precise bulk density measurements. The eleven TOIs that fall within this region are marked by an ‘x’. Also overplotted are planets with $\geq 3\sigma$ bulk density measurements from the literature that are classified as having either a rocky (circles), a gaseous (triangles), or an intermediate (squares) bulk composition. Marker colors are indicative of the MAP planet bulk densities.

ration or core-powered mass loss is less efficient around lower mass stars. This seems plausible in the photoevaporation scenario wherein the atmospheric mass loss rate is proportional to the XUV luminosity of the host star. X-rays in particular are the dominant driver of atmospheric mass loss by photoevaporation and observations have revealed that Sun-like stars have higher absolute X-ray luminosities than their low mass star counterparts (McDonald et al. 2019) despite the latter exhibiting a few to ten times larger L_X/L_{bol} ratios (Jackson et al. 2012; Shkolnik & Barman 2014).

Visual investigation of the occurrence rates of small close-in planets in the stellar mass bins considered by Fulton & Petigura 2018 (i.e. $M_s < 0.97 M_\odot$, $0.97 \leq M_s/M_\odot \leq 1.11$, and $M_s > 1.11 M_\odot$) suggests that the trend of increased filling of the valley with decreasing stellar mass may hold true (c.f. Figure 9; Fulton & Petigura 2018). However we emphasize that this hypothesis has not been tested rigorously. We also note that classical models of photoevaporation do not explicitly consider the effects of planetary magnetic fields on the efficiency of atmospheric mass loss and indeed the presence of such magnetic fields can partially stall atmospheric escape by varying amounts depending on the core composition of the planet (Owen & Adams 2019).

The simplest explanation for the imperfect clearing of the radius valley instead does not invoke that either gas-poor formation or atmospheric post processing is solely responsible for the valley’s formation. In comparing the slope of the radius valley around low mass and Sun-like stars (Figure 11), it is clear that the dominant process

affecting the slope of the valley with insolation evolves from a positive slope to a negative slope from Sun-like to low mass stars. However, the threshold M_s dividing each regime is unresolved such that the planet population considered herein likely features the superposition of processes such as gas-poor formation and thermally driven mass loss. The result of competing processes on the observed planet population could naturally explain the apparent partial filling of the gap.

8. SUMMARY OF MAIN FINDINGS

This study presented calculations of the occurrence rate of small close-in planets orbiting low mass stars using data from the *Kepler* and *K2* transit surveys. Our main findings are summarized below.

- The radius valley structure in the occurrence rate of small close-in planets—previously resolved around Sun-like stars—is demonstrated to persist around low mass stars (i.e. mid-K to mid-M dwarfs).
- The occurrence rate from considering confirmed *K2* planets only is likely underestimated. Although when *K2* planet candidates are included and statistically corrected for false positive contamination, the measured *Kepler* and *K2* cumulative occurrence rates of small close-in planets around low mass stars are in agreement: 2.48 ± 0.32 and 2.26 ± 0.38 planets per star respectively.
- The radius valley around low mass stars exhibits a negative slope with insolation ($r_{p,\text{valley}} \propto F^{-0.060 \pm 0.025}$) unlike around Sun-like stars whose measured slope is positive ($r_{p,\text{valley}} \propto F^{0.12 \pm 0.02}$; Martinez et al. 2019). This result supports models of gas-poor terrestrial planet formation without invoking atmospheric escape from photoevaporation, core-powered mass loss, or erosion by planetesimal impacts.
- The non-rocky planet peak in the bimodal occurrence rates is centered at $\sim 2 R_\oplus$ and effectively vanishes around mid-M dwarfs as rocky planets ($\lesssim 1.54 R_\oplus$) increasingly dominate the close-in planet population towards later spectral types. The relative fraction of rocky to non-rocky planets increases from $\sim 0.5 \pm 0.1 \rightarrow 8.5 \pm 4.6$ from mid-K to mid-M dwarfs.
- The occurrence rate-weighted location of the radius valley—and the central radius of each planet peak—shift to smaller sizes with decreasing stellar mass. The slope of the non-rocky planet peak’s central radius with stellar mass is twice that of the rocky peak’s slope indicating that the planet population in each stellar mass bin tends to converge towards rocky planet cores of $\sim 1 R_\oplus$ around later spectral types.
- Robust inferences to distinguish between various proposed physical mechanisms for the formation of the radius valley are expected to require $\mathcal{O}(85,000)$ mid-M dwarfs observed with 2-minute cadence with *TESS* or $\mathcal{O}(4700)$ mid-M dwarfs observed with

PLATO based on its expected performance and observing strategy.

- We advocate that transiting planets around stars with $T_{\text{eff}} < 4700$ K, and whose orbital periods and radii are situated between model predictions of the location of the rocky to non-rocky transition (see Figure 15), should be targeted by RV campaigns to resolve the location and slope of this transition with precise bulk density measurements.

We thank Martin Paegert for his efforts in contribut-

ing relevant data to and for his assistance in querying the *TESS* CTL database. We also thank Jennifer Winters and Jonathan Irwin for discussions regarding the population of nearby M dwarfs. We also thank Sam Quinn for discussions regarding past results from the *K2* mission. We also thank David Charbonneau for his thorough review of this manuscript. We thank the Canadian Institute for Theoretical Astrophysics for use of the Sunnyvale computing cluster throughout the early stages of this work. RC was supported by the Natural Sciences and Engineering Research Council of Canada and a grant from the National Aeronautics and Space Administration in support of the *TESS* science mission. KM is supported by the Natural Sciences and Engineering Research Council of Canada.

REFERENCES

- Aigrain, S., Hodgkin, S. T., Irwin, M. J., Lewis, J. R., & Roberts, S. J. 2015, MNRAS, 447, 2880 [4.2]
Aigrain, S., Parviainen, H., & Pope, B. J. S. 2016, MNRAS, 459, 2408 [4.2]
Akeson, R. L., Chen, X., Ciardi, D., et al. 2013, PASP, 125, 989 [3]
Astudillo-Defru, N., Cloutier, R., Wang, S. X., et al. 2020, arXiv e-prints, arXiv:2001.09175 [3, 13]
Bailer-Jones, C. A. L., Rybizki, J., Fouesneau, M., Mantelet, G., & Andrae, R. 2018, AJ, 156, 58 [2.2]
Barclay, T., Pepper, J., & Quintana, E. V. 2018, ArXiv e-prints, arXiv:1804.05050 [7.1]
Barnes, J. W. 2007, PASP, 119, 986 [4.4]
Barnes, R., & Greenberg, R. 2006, ApJL, 647, L163 [4.2]
Benneke, B., Werner, M., Petigura, E., et al. 2017, ApJ, 834, 187 [3]
Berger, T. A., Huber, D., Gaidos, E., & van Saders, J. L. 2018, ApJ, 866, 99 [1, 2.1, 1, 2.2]
Bonfils, X., Delfosse, X., Udry, S., et al. 2013, A&A, 549, A109 [6.2]
Bonfils, X., Almenara, J.-M., Cloutier, R., et al. 2018, A&A, 618, A142 [3]
Bouchy, F., Doyon, R., Artigau, É., et al. 2017, The Messenger, 169, 21 [7.2]
Bovy, J., Rix, H.-W., Green, G. M., Schlafly, E. F., & Finkbeiner, D. P. 2016, ApJ, 818, 130 [2.2]
Boyajian, T. S., von Braun, K., van Belle, G., et al. 2012, ApJ, 757, 112 [2.1, 2.2]
Burke, C. J., & Catanzarite, J. 2017, Planet Detection Metrics: Per-Target Flux-Level Transit Injection Tests of TPS for Data Release 25, Tech. rep. [4.1]
Burke, C. J., Christiansen, J. L., Mullally, F., et al. 2015, ApJ, 809, 8 [4.1]
Chen, H., & Rogers, L. A. 2016, ApJ, 831, 180 [1]
Chen, J., & Kipping, D. 2017, ApJ, 834, 17 [4.2]
Chiang, E., & Laughlin, G. 2013, MNRAS, 431, 3444 [6.1]
Choi, J., Dotter, A., Conroy, C., et al. 2016, ApJ, 823, 102 [2.2]
Christiansen, J. L., Clarke, B. D., Burke, C. J., et al. 2015, ApJ, 810, 95 [4.1, 4.1, 4]
—. 2016, ApJ, 828, 99 [4.1]
Christiansen, J. L., Vanderburg, A., Burt, J., et al. 2017, AJ, 154, 122 [4.1]
Claret, A., Hauschildt, P. H., & Witte, S. 2012, A&A, 546, A14 [4.2]
Cloutier, R. 2019, AJ, 158, 81 [4.2]
Cloutier, R., Astudillo-Defru, N., Bonfils, X., et al. 2019a, A&A, 629, A111 [3]
Cloutier, R., Astudillo-Defru, N., Doyon, R., et al. 2019b, A&A, 621, A49 [3]
Crossfield, I. J. M., Ciardi, D. R., Petigura, E. A., et al. 2016, ApJS, 226, 7 [5.3, 4]
Dittmann, J. A., Irwin, J. M., Charbonneau, D., Berta-Thompson, Z. K., & Newton, E. R. 2017a, AJ, 154, 142 [3]
Dittmann, J. A., Irwin, J. M., Charbonneau, D., et al. 2017b, Nature, 544, 333 [3]
Donati, J.-F., Kouach, D., Lacombe, M., et al. 2018, SPIRou: A NIR Spectropolarimeter/High-Precision Velocimeter for the CFHT, 107 [7.2]
Dressing, C. D., & Charbonneau, D. 2013, ApJ, 767, 95 [1]
—. 2015, ApJ, 807, 45 [1, 3, 4.2, 5.1, 5.4]
Dressing, C. D., Charbonneau, D., Dumusque, X., et al. 2015, ApJ, 800, 135 [1]
Dressing, C. D., Vanderburg, A., Schlieder, J. E., et al. 2017, AJ, 154, 207 [5.3, 4]
Eker, Z., Bakış, V., Bilir, S., et al. 2018, MNRAS, 479, 5491 [6.3]
Fressin, F., Torres, G., Charbonneau, D., et al. 2013, ApJ, 766, 81 [1]
Fulton, B. J., & Petigura, E. A. 2018, AJ, 156, 264 [1, 6.3, 13, 6.3, 7.2, 7.3]
Fulton, B. J., Petigura, E. A., Howard, A. W., et al. 2017, AJ, 154, 109 [1, 2, 1, 2.2, 4.1, 7.3]
Gaidos, E., Mann, A. W., Kraus, A. L., & Ireland, M. 2016, MNRAS, 457, 2877 [1, 2.1, 3, 5.1, 5.4]
Gillon, M., Demory, B.-O., Van Grootel, V., et al. 2017, Nature Astronomy, 1, 0056 [3]
Ginzburg, S., Schlichting, H. E., & Sari, R. 2018, MNRAS, 476, 759 [1]
Gupta, A., & Schlichting, H. E. 2019a, MNRAS, 487, 24 [1]
—. 2019b, arXiv e-prints, arXiv:1907.03732 [1, 5, 11, 6.1, 13, 6.3]
Hamann, A., Montet, B. T., Fabrycky, D. C., Agol, E., & Kruse, E. 2019, AJ, 158, 133 [3]
Hardegree-Ullman, K. K., Cushing, M. C., Muirhead, P. S., & Christiansen, J. L. 2019, AJ, 158, 75 [1, 6.2]
Harpsoe, K. B. W., Hardis, S., Hinse, T. C., et al. 2013, A&A, 549, A10 [3]
Henry, T. J., & McCarthy, Jr., D. W. 1993, AJ, 106, 773 [2.1]
Hirano, T., Dai, F., Gandolfi, D., et al. 2018, AJ, 155, 127 [5.3, 4]
Howard, A. W., Marcy, G. W., Bryson, S. T., et al. 2012, ApJS, 201, 15 [1]
Howell, S. B., Sobeck, C., Haas, M., et al. 2014, PASP, 126, 398 [4.2]
Huber, D., Zinn, J., Bojsen-Hansen, M., et al. 2017, ApJ, 844, 102 [2.1]
Jackson, A. P., Davis, T. A., & Wheatley, P. J. 2012, MNRAS, 422, 2024 [1, 7.3]
Jenkins, J. M., Chandrasekaran, H., McCauliff, S. D., et al. 2010, in SPIE, Vol. 7740, Software and Cyberinfrastructure for Astronomy, 77400D [4.1]
Jenkins, J. M., Twicken, J. D., McCauliff, S., et al. 2016, in SPIE, Vol. 9913, Software and Cyberinfrastructure for Astronomy IV, 99133E [7.1]
Jin, S., & Mordasini, C. 2018, ApJ, 853, 163 [1]
Jin, S., Mordasini, C., Parmentier, V., et al. 2014, ApJ, 795, 65 [1]
Kass, R. E., & Raftery, A. E. 1995, Journal of the American Statistical Association, 90, 773 [7]
Kite, E. S., Fegley, Bruce, J., Schaefer, L., & Ford, E. B. 2019, ApJ, 887, L33 [6.2]

- Koch, D. G., Borucki, W. J., Basri, G., et al. 2010, *ApJ*, 713, L79 [4.1]
- Kostov, V. B., Schlieder, J. E., Barclay, T., et al. 2019, *AJ*, 158, 32 [3]
- Kotani, T., Tamura, M., Suto, H., et al. 2014, in SPIE, Vol. 9147, Ground-based and Airborne Instrumentation for Astronomy V, 914714 [7.2]
- Kreidberg, L. 2015, *PASP*, 127, 1161 [4.2]
- Kruse, E., Agol, E., Luger, R., & Foreman-Mackey, D. 2019, *ApJS*, 244, 11 [5.3, 5.3, 5.4, 10]
- Lee, E. J., & Chiang, E. 2016, *ApJ*, 817, 90 [1, 6.1]
- Lee, E. J., Chiang, E., & Ormel, C. W. 2014, *ApJ*, 797, 95 [1, 6.1]
- Li, J., Tenenbaum, P., Twicken, J. D., et al. 2018, arXiv e-prints, arXiv:1812.00103 [7.1]
- Lindgren, L., Hernández, J., Bombrun, A., et al. 2018, *A&A*, 616, A2 [2.1]
- Livingston, J. H., Crossfield, I. J. M., Petigura, E. A., et al. 2018, *AJ*, 156, 277 [5.3, 4]
- Lopez, E. D., & Fortney, J. J. 2014, *ApJ*, 792, 1 [1]
- Lopez, E. D., & Rice, K. 2018, *MNRAS*, 479, 5303 [1, 6.1, 5, 11, 13, 6.3]
- Luger, R., Agol, E., Kruse, E., et al. 2016, *AJ*, 152, 100 [4.2]
- Luger, R., Kruse, E., Foreman-Mackey, D., Agol, E., & Saunders, N. 2018, *AJ*, 156, 99 [4.2]
- Lundkvist, M. S., Kjeldsen, H., Albrecht, S., et al. 2016, *Nature Communications*, 7, 11201 [3, 5.1]
- Luque, R., Pallé, E., Kossakowski, D., et al. 2019, *A&A*, 628, A39 [3]
- MacDonald, M. G., Ragozzine, D., Fabrycky, D. C., et al. 2016, *AJ*, 152, 105 [3]
- Mahadevan, S., Ramsey, L., Bender, C., et al. 2012, in SPIE, Vol. 8446, Ground-based and Airborne Instrumentation for Astronomy IV, 84461S [7.2]
- Mamajek, E. E., Torres, G., Prsa, A., et al. 2015, arXiv e-prints, arXiv:1510.06262 [2.2]
- Mandel, K., & Agol, E. 2002, *ApJL*, 580, L171 [4.2]
- Mann, A. W., Feiden, G. A., Gaidos, E., Boyajian, T., & von Braun, K. 2015, *ApJ*, 804, 64 [2.1, 2.2]
- Martinez, C. F., Cunha, K., Ghezzi, L., & Smith, V. V. 2019, *ApJ*, 875, 29 [1, 6.1, 5, 11, 6.1, 7.2, 7.3, 15, 8]
- Mathur, S., Huber, D., Batalha, N. M., et al. 2017, *ApJS*, 229, 30 [2.1]
- Mayo, A. W., Vanderburg, A., Latham, D. W., et al. 2018, *AJ*, 155, 136 [5.3, 4]
- Mazeh, T., Holczer, T., & Faigler, S. 2016, *A&A*, 589, A75 [3, 5.1]
- McDonald, G. D., Kreidberg, L., & Lopez, E. 2019, *ApJ*, 876, 22 [7.3]
- Ment, K., Dittmann, J. A., Astudillo-Defru, N., et al. 2019, *AJ*, 157, 32 [3]
- Montet, B. T., Morton, T. D., Foreman-Mackey, D., et al. 2015, *ApJ*, 809, 25 [5.3, 4]
- Morales, J. C., Mustill, A. J., Ribas, I., et al. 2019, *Science*, 365, 1441 [6.2]
- Morton, T. D. 2012, *ApJ*, 761, 6 [5.3]
- . 2015, VESPA: False positive probabilities calculator, Astrophysics Source Code Library, ascl:1503.011 [5.3]
- Morton, T. D., & Swift, J. 2014, *ApJ*, 791, 10 [1, 3, 5.1, 5.4]
- Mulders, G. D., Pascucci, I., & Apai, D. 2015a, *ApJ*, 798, 112 [1, 6.3]
- . 2015b, *ApJ*, 814, 130 [6.3]
- Neil, A. R., & Rogers, L. A. 2018, *ApJ*, 858, 58 [6.3]
- . 2019, arXiv e-prints, arXiv:1911.03582 [6.3]
- Owen, J. E., & Adams, F. C. 2019, *MNRAS*, 490, 15 [7.3]
- Owen, J. E., & Wu, Y. 2013, *ApJ*, 775, 105 [1]
- . 2017, *ApJ*, 847, 29 [1]
- Pecaut, M. J., & Mamajek, E. E. 2013, *ApJs*, 208, 9 [2]
- Petigura, E. A., Howard, A. W., & Marcy, G. W. 2013, Proceedings of the National Academy of Science, 110, 19273 [1]
- Petigura, E. A., Howard, A. W., Marcy, G. W., et al. 2017, *AJ*, 154, 107 [2.1]
- Petigura, E. A., Marcy, G. W., Winn, J. N., et al. 2018, *AJ*, 155, 89 [4.1]
- Quirrenbach, A., Amado, P. J., Caballero, J. A., et al. 2014, in SPIE, Vol. 9147, Ground-based and Airborne Instrumentation for Astronomy V, 91471F [7.2]
- Rauer, H., Catala, C., Aerts, C., et al. 2014, *Experimental Astronomy*, 38, 249 [7.1]
- Rice, K., Malavolta, L., Mayo, A., et al. 2019, *MNRAS*, 484, 3731 [3]
- Ricker, G. R., Winn, J. N., Vanderspek, R., et al. 2015, *Journal of Astronomical Telescopes, Instruments, and Systems*, 1, 014003 [7.1]
- Rogers, L. A. 2015, *ApJ*, 801, 41 [1]
- Schllichting, H. E., Sari, R., & Yalinewich, A. 2015, *Icarus*, 247, 81 [1]
- Seifahrt, A., Stürmer, J., Bean, J. L., & Schwab, C. 2018, ArXiv e-prints, arXiv:1805.09276 [7.2]
- Shkolnik, E. L., & Barman, T. S. 2014, *AJ*, 148, 64 [7.3]
- Shuvalov, V. 2009, *Meteoritics and Planetary Science*, 44, 1095 [1]
- Stassun, K. G., Oelkers, R. J., Paegert, M., et al. 2019, *AJ*, 158, 138 [7.1]
- Twicken, J. D., Catanzarite, J. H., Clarke, B. D., et al. 2018, *Publications of the Astronomical Society of the Pacific*, 130, 064502 [7.1]
- Valencia, D., Guillot, T., Parmentier, V., & Freedman, R. S. 2013, *ApJ*, 775, 10 [5.1]
- Van Eylen, V., Agentoft, C., Lundkvist, M. S., et al. 2018, *MNRAS*, 479, 4786 [1, 5.1, 8, 7.3]
- Vanderburg, A., & Johnson, J. A. 2014, *PASP*, 126, 948 [4.2]
- Weiss, L. M., & Marcy, G. W. 2014, *ApJL*, 783, L6 [1, 3]
- Winters, J. G., Henry, T. J., Jao, W.-C., et al. 2019, *AJ*, 157, 216 [7.1]
- Wu, Y. 2019, *ApJ*, 874, 91 [1, 5.1, 8, 13, 6.3, 7.2]
- Wyatt, M. C., Kral, Q., & Sinclair, C. A. 2019, arXiv e-prints, arXiv:1910.10731 [1, 5]
- Youdin, A. N. 2011, *ApJ*, 742, 38 [1]
- Zeng, L., & Sasselov, D. 2013, *PASP*, 125, 227 [5.1]
- Zeng, L., Sasselov, D. D., & Jacobsen, S. B. 2016, *ApJ*, 819, 127 [6.1]
- Zhu, W., Petrovich, C., Wu, Y., Dong, S., & Xie, J. 2018, *ApJ*, 860, 101 [5.1]
- Zink, J. K., Hardegree-Ullman, K. K., Christiansen, J. L., et al. 2020, arXiv e-prints, arXiv:2001.11515 [4.2, 5.4]